

## Abstract

ZEIGLER, GARY BOYCE, II. Direct Detection of Microcalcification Pairs in Simulated Digital Mammograms. (Under the Direction of Professor Kuruvilla Verghese.)

Using the MCMIS (Monte Carlo for Mammography Image Simulation) code, several possible scenarios of microcalcification images were simulated for the Fischer Senoscan<sup>TM</sup> digital mammography system, which has been approved for clinical use by the F.D.A. The cases simulated included detectors that have 100  $\mu\text{m}$  x 100  $\mu\text{m}$ , 50  $\mu\text{m}$  x 50  $\mu\text{m}$ , and 25  $\mu\text{m}$  x 25  $\mu\text{m}$  pixels in order to determine how much improvement can be obtained through decreased pixel size in the detection of microcalcification clusters in mammograms. Breast thickness was also varied for each modality from 4 to 7 cm in order to determine the effect that reduced breast compression will have on image quality under ideal conditions. The breast phantom used for each simulation included a region of microcalcification pairs of varying size and pair spacing. This microcalcification cluster phantom was designed such that simulated images would indicate the minimum required size and spacing for microcalcification clusters to become distinctly discernable in each of the modalities under scrutiny. Both qualitative and quantitative analyses were performed for each simulated image produced. A decrease in detector pixel size did not show the expected result of significant improvement in cluster detection ability, even under ideal conditions. However, for the range of breast thickness studied, results indicate that decreasing the amount of compression during a mammogram did not significantly affect the image quality in terms of image resolution or contrast for all detector modalities tested. These results suggest that new detector modalities incorporating smaller detector pixel sizes may not show significant improvement over current modalities. However, they also suggest that doctors may be able

to make the mammogram process less painful for the patient while maintaining image quality.

# Direct Detection of Microcalcification Pairs in Simulated Digital Mammograms

By

**Gary B. Zeigler, II**

A thesis submitted to the Graduate Faculty of  
North Carolina State University  
in partial fulfillment of the  
requirements for the Degree of  
Master of Science

**Department of Nuclear Engineering**

Raleigh, North Carolina  
2002

**Approved by:**

---

Dr. J. Michael Doster

---

Dr. Zhilin Li

---

Dr. R. Eugene Johnston

---

Dr. Douglas E. Peplow

---

Dr. Kuruvilla Verghese, Chair

This work is dedicated in memory of

**Doris Anne Boeshans Owen,**

my loving grandmother and a victim of breast cancer.

## Biography

Gary B. Zeigler, II was born November 25, 1977 in Greensboro, North Carolina. He grew up primarily in Whitsett, North Carolina with his mother and stepfather, Mary and Ronald Key, as well as his two stepbrothers, Eric and Ryan. He spent his first three years of primary school at Our Lady of Grace Catholic School in Greensboro, and the remainder of his primary and secondary education in Guilford County public schools. Gary graduated first in his class in May of 1996 from Eastern Guilford High School. The following fall, he began college at North Carolina State University as a nuclear engineering undesignated student. While attending NCSU as an undergraduate, Gary worked as a tutor for student athletes, was an undergraduate research assistant in the Nuclear Engineering department, participated extensively in the Nuclear Engineering Outreach Program, and worked as the NE department librarian. After obtaining his B.S. in Nuclear Engineering in May of 2000, he began his graduate study in Nuclear Engineering at NCSU.

# Table of Contents

	Page
List of Tables .....	vi
List of Figures .....	vii
1. Introduction .....	1
2. Mammography Simulation Using Monte Carlo .....	6
2.1 Monte Carlo Use in Mammography Simulation .....	6
2.2 Microcalcifications in Mammography .....	8
2.3 Use of the MCMIS Monte Carlo Code for Image Simulation .....	12
2.3.1 Microcalcification Phantom .....	13
2.3.2 Breast Phantom .....	16
2.3.3 Source and Detector Set-up .....	17
2.3.4 Other MCMIS Parameters .....	20
3. Image Production and Analysis .....	23
3.1 Image Production .....	23
3.1.1 Weighting Contributions from Monoenergetic MCMIS Runs .....	25
3.1.2 Addition of Weighted Images .....	25
3.1.3 Scatter Map Interpolation .....	27
3.1.4 Smearing the Image with the System MTF .....	27
3.2 Production and Implementation of Analysis Tools .....	28
3.2.1 Calculation of Resolution .....	29
3.2.2 Calculation of Contrast .....	35
4. Discussion of Image Analysis .....	36
4.1 Resolution Effects .....	36
4.1.1 Effect of Decreased Pixel Dimensions on Image Resolution .....	37
4.1.2 Effect of Increased Breast Thickness on Image Resolution .....	42
4.2 Contrast Effects .....	44
4.2.1 Effect of Decreased Pixel Dimensions on Image Contrast .....	47
4.2.2 Effect of Increased Breast Thickness on Image Contrast .....	49
5. Summary and Conclusions .....	52
6. Bibliography .....	55

7. Appendices .....	58
I. User Defined Input for MCMIS .....	59
I.1 Materials .....	60
I.2 Geometry .....	61
I.3 Source and Detector .....	65
I.4 Monte Carlo Parameters .....	68
II. Image Production and Analysis Codes .....	71
II.1 Image Production Code .....	71
II.1.1 Algorithm .....	71
II.1.2 Code .....	72
II.2 Additional Images .....	80
II.3 Image Analysis Codes .....	90
II.3.1 Algorithm for Calculating Resolution .....	90
II.3.2 Code for Calculating Resolution .....	91
II.3.3 Algorithm for Calculating Contrast .....	93
II.3.4 Code for Calculating Contrast .....	94

## List of Tables

	Page
Table 4.1 Minimum threshold values in the smeared images from each detector type used.	46
Table I.1 The seven basic shapes for the geom.inp file and their associated parameters. ...	61
Table I.2 Available source types for the sode.inp input file and their associated parameters. .....	66
Table I.3 Available detector types for the sode.inp input file ant their associated parameters. . .....	67
Table I.4 Phosphor types available for the sode.inp file with appropriate density thickness and thickness values (where applicable). ....	67
Table I.5 Description of the 5 logical statements necessary for the mc.inp input file. ....	69

## List of Figures

	Page
Figure 2.1 Top view of microcalcification cluster phantom used in MCMIS simulations. . .	15
Figure 2.2 Side view of breast phantoms used in the MCMIS simulations with microcalcification phantom shown in each breast for (a) 4 cm, (b) 5 cm, (c) 6 cm, and (d) 7 cm breast thicknesses. ....	18
Figure 2.3 The Fischer Senoscan™ scanning slot digital mammography unit. ....	19
Figure 3.1 Source spectrum used to simulate images produced by the Fischer Senoscan™ system. ....	24
Figure 3.2 Weight vs. MC Energy. ....	26
Figure 3.3 A microcalcification cluster from the image produced using a 100- $\mu\text{m}$ pixel detector and a 4-cm breast thickness. ....	29
Figure 3.4 Pixel values for a single row of pixels in the center of a row of microcalcifications (A “line scan”) in an unsmearred image. ....	32
Figure 3.5 Line scan for a smearred image. ....	33
Figure 3.6 Three steps used to determine area in which microcalcification is located. ....	34
Figure 4.1 Unsmearred images produced with a breast thickness of 4 cm. ....	38
Figure 4.2 Smearred images produced with a breast thickness of 4 cm. ....	39
Figure 4.3 Maximum fraction of microcalcifications visible versus breast thickness. ....	40
Figure 4.4 Maximum fraction of microcalcifications visible versus breast thickness. ....	41
Figure 4.5 Unsmearred images produced with a pixel size of 25 $\mu\text{m}$ . ....	43
Figure 4.6 Smearred images produced with a pixel size of 25 $\mu\text{m}$ . ....	44
Figure 4.7 Total image contrast data for each breast thickness for the 25- $\mu\text{m}$ pixel detector as a function of user defined threshold. ....	45
Figure 4.8 Fraction of microcalcifications detected versus the contrast determined at a given threshold. ....	47

Figure 4.9 Contrast versus detector pixel size for varied breast thickness. ....	48
Figure 4.10 Contrast versus detector pixel size for varied breast thickness. ....	49
Figure 4.11 Contrast versus breast thickness for three different detectors. ....	50
Figure 4.12 Contrast versus breast thickness for three different detectors. ....	51
Figure II.1 Images of a 4 cm breast produced using a 50 $\mu\text{m}$ pixel detector. ....	81
Figure II.2 Images of a 5 cm breast produced using a 100 $\mu\text{m}$ pixel detector. ....	82
Figure II.3 Images of a 5 cm breast produced using a 50 $\mu\text{m}$ pixel detector. ....	83
Figure II.4 Images of a 5 cm breast produced using a 25 $\mu\text{m}$ pixel detector. ....	84
Figure II.5 Images of a 6 cm breast produced using a 100 $\mu\text{m}$ pixel detector. ....	85
Figure II.6 Images of a 6 cm breast produced using a 50 $\mu\text{m}$ pixel detector. ....	86
Figure II.7 Images of a 6 cm breast produced using a 25 $\mu\text{m}$ pixel detector. ....	87
Figure II.8 Images of a 7 cm breast produced using a 100 $\mu\text{m}$ pixel detector. ....	88
Figure II.9 Images of a 7 cm breast produced using a 50 $\mu\text{m}$ pixel detector. ....	89

# Chapter 1

## Introduction

Breast cancer incidence rate among U.S. women is about one in nine. Early detection of breast cancer is essential in saving lives and currently, x-ray mammography is considered the best-established diagnostic tool for tumor detection in the breast. Although controversial, the U.S. government has recently reiterated the recommendation to screen women over 40 using x-ray mammography. Despite the many advances achieved in mammography, the false negative rates remain undesirably high, particularly among pre-menopausal women. One of the reasons for low contrast between tumor and breast tissue is the contrast degradation caused by the contribution of scattered photons to the image. However, newer digital mammography scanners have been designed and tested which eliminate much of the scattered photon contribution. Several such machines are now appearing at medical facilities.

Another reason for the contrast problem is the inherently small density difference, of the order of just a few percent, between the tumor and the breast tissue. This problem is even more acute in women under the age of 50 since the pre-menopausal woman has a dominant amount of dense, glandular breast tissue, rather than the less dense, fatty tissue found in older women. When diagnosis is difficult due to such contrast problems, radiologists typically look for other indicators of potential problem, one such indicator being clusters of microcalcifications.

Among malignant tumors in the breast, 50% to 70% are estimated to contain clusters of microcalcifications, which are small deposits of calcium compounds (mostly oxalates)

varying in size from 100  $\mu\text{m}$  (or even less) to about 400  $\mu\text{m}$  (Herman *et al* 1988). In early stages of carcinoma, these microcalcification clusters are sometimes the only indicator of problems. Herman *et al* also suggest that if grouped microcalcifications are found in the absence of a readily observable tumor, a detailed investigation of the region in which they occur should be thoroughly pursued. Therefore, it is believed that the ability to discern individual calcifications within clusters in x-ray mammograms will serve as a marker for breast cancer in mammograms where the tumors themselves may not be convincingly visible.

As a follow-up to previous efforts at assessing the performance of new mammography modalities through image simulation by Monte Carlo, we are now studying the potential for imaging of microcalcification cluster patterns by a relatively new digital mammography system, namely, the Fischer Senoscan<sup>TM</sup>. Spatial resolution of calcification clusters in a mammogram is affected by the hardware and the operating parameters of the system, as well as by the size, composition and architecture of the breast. The major hardware item that affects spatial resolution is the inherent pixel dimensions of the digital detector. Some of the detector systems currently used in clinical settings use 100  $\mu\text{m}$  pixels, while the Senoscan<sup>TM</sup> uses 50  $\mu\text{m}$  pixels. Some experimental detectors have even achieved a pixel size as small as 25  $\mu\text{m}$ . The kVp of the x-ray tube will also affect the resolution and contrast because of changes in photon scattering. The first task of this thesis work is to quantify the changes in contrast and resolution when using detectors with pixel sizes characteristic to the Senoscan<sup>TM</sup> device, as well as other detectors not commonly used in today's x-ray mammography systems.

Similarly, breast thickness and its glandular tissue/fat content can also change the scattering effects, thus affecting both contrast and resolution. One of the factors that

discourage women from getting routine screening is the pain associated with the degree of breast compression that is necessary for current mammography systems. It may, therefore, be beneficial if the degree of compression can be reduced, as women will find a somewhat relaxed amount of compression more acceptable. A small degree of compression is essential in order to immobilize the breast. As a first approximation, compression only changes the shape of the breast and not its density. Therefore, it is believed that the loss of resolution and contrast from varying breast size in simulation studies can serve as an indication of the effect of reduced compression in those cases where the calcification clusters are in the central region of the breast. Thus, the second task set upon in this thesis is to quantify the resolution and contrast effects on simulated radiographs due to changes in breast thickness.

In order to investigate these aspects of digital mammography, this study makes use of the MCMIS Monte Carlo simulation code written and benchmarked by Douglas Peplow (Peplow 1999) while he was a doctoral student at North Carolina State University. The MCMIS code calculates images and radiation dose profiles for two different mammography modalities, one of which is the Senoscan™. The simulated source of x-rays is a high intensity x-ray tube operated at about 40 kVp. The low energy photons (those below 5 keV) are filtered out, while the rest are collimated through a slot collimator to produce effectively a line source. The breast is compressed between two curved paddles. Below the lower paddle is a detector with a line CCD array. The collimator slot at the source and the detector scan across the breast to produce a digital radiograph of the breast.

The simulation studies described here are based on a microcalcification phantom embedded in the MCMIS breast model. A small computational phantom of microcalcifications of different sizes was designed and placed within the simulated breast.

The phantom consists of pairs of different sizes of calcifications, with each pair separated by a given distance. The details of the calcification phantom are shown in Chapter 2.

Simulated images of the microcalcification phantom in a breast consisting of 50% glandular/50% fatty tissue (typical assumed composition for older women) for breast thickness ranging from 4 cm to 7 cm have been generated for the standard operating conditions of the Senoscan™ tube. These simulated images are used to assess the effects of reducing pixel size and decreasing breast compression.

The remainder of this work is divided into 4 main chapters. Chapter 2 includes some background information on the general use of Monte Carlo in mammography simulation. Also, some information on microcalcifications and their importance in mammography is discussed in greater detail. Finally, a detailed description of the use of the MCMIS Monte Carlo Code for this work is discussed.

Chapter 3 discusses actual image simulation and processing, as well as analysis of the output from the MCMIS Code. This section includes a detailed description of how simulated images are produced using Matlab™ to process the output from MCMIS. Then, a discussion of the analysis of these images is included. Finally, the development of a quantitative comparison of images is described.

Chapter 4 includes discussion based on actual comparisons of the various images produced and findings from these comparisons. Effects of varied pixel size and varied breast thickness are discussed, with emphasis on resolution differences for varied pixel sizes, and both resolution and contrast differences for varied breast thickness.

Finally, Chapter 5 summarizes the work, and presents the conclusions drawn from the analyses made in Chapters 3 and 4. Also, two appendices are included at the end of this

work. The first includes information on the input used in the MCMIS code for this work.

The last appendix includes all relevant figures and computer codes not included in the main body of the work.

## Chapter 2

# Mammography Simulation Using Monte Carlo

This chapter gives background information on three areas vital to this work. The first is a literature review of diagnostic radiology and mammography simulation using Monte Carlo techniques. The second focal point of this chapter is microcalcifications and their role in mammography screening. Lastly, a detailed description is given of the MCMIS Monte Carlo Code as it was used in this work, which includes discussion on both input parameters used and development of the microcalcification phantom.

## 2.1 Monte Carlo Use in Mammography Simulation

Use of X-rays to perform diagnostic radiography of the internal body has been used for the better part of a century. To make improvements to such systems, it is necessary to study the factors that influence an imaging system, including the effects of radiation exposure to the patients themselves. Experimental methods to investigate these factors are often very difficult or even impossible to employ due to the difficulty of experimentation by varying every parameter individually (Morin 1988). When considering radiation exposure to the patient, not only the physical limitations of experimental studies become evident, but also the advisability of exposing patients to radiation for the purpose of study becomes readily evident.

Monte Carlo simulation methods have proven themselves extraordinarily useful in the area of diagnostic radiography for performing parametric evaluations. Use of MC codes

allows for a wide range of study independent of the physical limitations of the imaging system, since the photon physics are inherent in the code itself. The radiation damage issues, too, are avoided as MC codes make use of “phantom” patients, which allow scientists to study the effects of radiation on tissue without subjecting living patients to any radiation exposure at all. Also, the nature of almost all MC codes used in diagnostic radiography allows users to vary input parameters in order to study the effects of various radiological environments that one may come across in the institutional setting.

It is not surprising, then, that one of the major areas of interest in diagnostic radiology, mammography, should make use of MC methods. Within the last 15 years, MC has been used extensively for dose modeling and, to a lesser extent, image simulation. As Peplow and Verghese (1999) point out, earlier works in this area have been lacking in that they did not include full 3-D imaging effects or were limited in their analysis of a system, focusing only on one or two aspects of the imaging system. They were, however, able to demonstrate the effects of varied air gap thickness or source energy. However, a more recent code, called “MCMIS”, has been developed and has demonstrated the ability to create accurate simulated mammography images that include full 3-D effects, includes dose modeling within all regions of interest within the target phantom, and is able to produce data for polyenergetic X-ray systems within an acceptable amount of time. A more detailed description of the code and the benchmarking of the code can be found in the doctoral dissertation of Peplow (1999).

The MCMIS code, therefore, is a highly useful tool for analyzing various parameters inherent to mammography systems. For this work, in particular, the MCMIS code allows the simulation of images for the Fischer Senoscan™ for varied detector pixel dimensions and

breast thickness. These comparisons allow us to see what benefits are possible for improvements in a given system, as well as what kinds of changes may be made to current mammography modalities to improve not only image quality, but also patient comfort.

## 2.2 Microcalcifications in Mammography

In mammography, one of the primary indicators that radiologists look for when determining whether or not a cancerous tumor is present are clusters of tiny deposits of calcium called microcalcifications. Calcium deposits occur naturally in all breasts, and the appearance of a calcification in the radiograph of a breast does not correlate with the existence of carcinoma. However, clusters of microcalcifications (i.e. calcifications of size less than 500  $\mu\text{m}$ ) can be a very good indicator of the presence of a cancerous region. As mentioned in the introduction, somewhere between 50% and 70% of malignant tumors are accompanied by clusters of microcalcifications (Herman *et al* 1988). The shape and contrast features of microcalcifications can also be very important in determining whether a cancer is benign or malignant, and are therefore often used in the detection algorithms of Computer-Aided Diagnosis (CAD) schemes (Veldkamp and Karssemeijer 1998).

However, as mentioned by Lado *et al* (1997), microcalcifications are commonly missed in mammography screening due to their appearance as extremely small, low contrast entities many times located in very inhomogeneous regions. Many of these microcalcifications are much smaller than current detector or image pixel size at only several  $\mu\text{m}$  in size. Most current detectors or digitized images of screen-film mammograms have at best 50  $\mu\text{m}$  pixel size, with others having larger pixel sizes of 100  $\mu\text{m}$ . Therefore, physicians may request that a colleague also view a mammogram in order to verify a suspected cluster

of microcalcifications (Nagel *et al* 1998). Also, the use of CAD schemes can be employed in order to have a third “reading” done by a code designed to locate potential regions of microcalcification clusters. The majority of work done in the area of microcalcification detection in mammography has been in either the area of CAD design, implementation, and optimization, or in the area of improved digitization of screen-film mammograms.

Some of the earliest work in this area dealt primarily with the digitization of screen-film mammograms in order to improve methods of storage, processing, display, and transfer of images. In a study performed by Chan *et al* (1987), the resolution requirements and unsharp-mask filtering effects on detection of microcalcification clusters were discussed. This study found that the digitization of screen-film images to 100  $\mu\text{m}$  reduced the ability of readers to detect microcalcifications due to losses in spatial resolution and increase in quantization noise. It was also noted that at that time, the digitizer used had much greater spatial resolution than could be achieved by direct digital systems. This, they suggested, meant that direct digital systems might need to have high spatial resolution combined with very low noise to produce images even near the same quality as screen-film systems. They also suggested that when proper processing techniques, such as sharp-mask filtering, were used, the spatial resolution requirements for digital images might be reduced from that of a screen-film system. However, even with processing techniques, the study concluded that the number of false-positive microcalcification clusters detected increased, even when the processed image was presented with the unprocessed image.

One of the other areas of mammogram digitization that proved problematic was image compression. In order to decrease the large size of digitized images so that image files could be more easily and rapidly transferred, compression techniques were necessary that

would not decrease image quality to a significant degree. Another study by Chan *et al* (1996) discussed the comparison of two methods of image compression – discrete cosine transform-full frame entropy coding (DCT-FFEC) and Laplacian pyramid hierarchical coding (LPHC). Using the CAD algorithm developed by the group, the DCT-FFEC method was shown to be more efficient than LPHC at image compression. The highest compression ratio achieved without significant reduction in image quality was 9.6:1, which means approximately an order of magnitude reduction in image file size. This study, however, still reported that digitized images with 100  $\mu\text{m}$  pixel sizes still reduced the ability of radiologists to accurately detect microcalcification clusters, and that CAD detection accuracy was reduced at any pixel size over 35  $\mu\text{m}$ .

Many studies have also been done to improve the performance of CAD systems. Qian *et al* (1994) made use of quadrature mirror filter banks (QMF) with multiple channels and were able to significantly improve CAD analysis over the use of the commonly applied tree structured wavelet transforms (TSWT). Their study showed that using the QMF filter with 3 channels on 15 mammograms digitized at a resolution of 105  $\mu\text{m}$  per pixel allowed their CAD system to correctly extract microcalcification clusters with a true positive rate of 100%, and an average of 0.6 false positive microcalcification clusters per mammogram. The author did not provide information, however, on the actual size of microcalcifications visible in the mammograms used.

Another study performed by Yoshida *et al* (1996) also focused on improvement of CAD systems. This study incorporated a wavelet transform technique combined with a difference-image technique, which resulted in a true positive rate of 95% and a false positive rate of 1.5 microcalcification clusters per mammogram. The 39 mammograms used in this

study were digitized at a resolution of 100  $\mu\text{m}$  with an average microcalcification diameter of 300  $\mu\text{m}$ . Later work on this project was able to improve the method used even more by optimization of the weights used for the wavelet transforms (Zhang *et al* 1998).

Another study on improving the detection of microcalcification clusters by CAD systems by removing false positives used a combination of a rule based feature analysis and an artificial neural network (ANN) (Nagel *et al* 1998). This study compared this combination of methods to use of each method separately. The methods were applied to two different databases of actual mammograms, a first that contained 39 mammograms digitized at 100  $\mu\text{m}$  pixels, and a second that contained 50 digitized mammograms. Microcalcification diameters for the first database are reported as  $300 \pm 300 \mu\text{m}$ . For the first database, optimum results achieved were 0.17 false positives per mammogram for the combined method, 0.22 for the rule-based method alone, and 0.38 for the ANN method alone. For the 50 image database, the average number of false positives per mammogram was 0.8 for the combined method, 1.9 for the rule-based method alone, and 1.6 for the ANN method alone. These results showed that the combined method was indeed superior to either rule-based or ANN methods applied independently.

Another area of interest that has played an important role in the use of CAD methods is development of accurate segmentation methods. Segmentation refers to the method in which the exact size and shape of an object in a mammogram is determined. It is immediately obvious that this will play an important role in determining spatial resolution and contrast for a particular mammography modality. The work of Veldkamp and Karssemeijer (1998) found that both local noise dependent threshold and fixed contrast threshold methods were very poor compared to the other two methods employed, which were

a signal dependent threshold method or an iterative method based on the Markov random field model. However, both of the latter methods still overestimated the size of the microcalcifications used in their phantom that were in the range 200 to 400  $\mu\text{m}$ , while only those larger than this range were accurately estimated. This is somewhat troubling since microcalcifications are generally in this size range.

Some more recent work has focused less on CAD systems and has started to look towards comparison of direct digital systems with screen-film systems. For example, current direct digital systems have been shown to produce radiographs with as high quality as certain screen-film systems. One such work on this has shown the ability of observers to detect simulated microcalcifications as small as 130  $\mu\text{m}$  equally well in both direct digital and screen-film systems under scatter free conditions (Cowen *et al* 1997). The authors then went on to say that at low exposures, the detection ability of observers was found to be the same, but at high exposures, the direct digital system proved better as observers could even detect simulated microcalcifications down to 110  $\mu\text{m}$ , while the screen-film observations deteriorated to only 170  $\mu\text{m}$  microcalcifications. This study also discussed the ability of observers to determine shapes of test details in both screen-film systems and direct digital systems. For smaller simulated microcalcifications, the authors report that observers were still better able to determine the shape of microcalcifications using the screen-film mammograms.

## 2.3 Use of the MCMIS Monte Carlo Code for Image Simulation

As discussed previously, many past works focus primarily on digital mammography in the sense of digitized screen-film mammograms rather than direct digital mammography

systems. The work of Cowen *et al* (1997) focused on the comparison between direct digital systems and screen-film systems and showed promising results for direct digital systems that use 100  $\mu\text{m}$  pixel detectors. The work presented here addresses some issues neglected in many of the past studies conducted in the area of microcalcification detection in mammography by looking at how well some of the more recent direct digital systems work. Specifically, we will address three major topics associated with the performance of mammography systems. These three topics are detector resolution, contrast, and effects on image quality due to breast compression. Since more recent direct digital systems are utilizing even smaller pixel sizes of 50  $\mu\text{m}$ , significant improvements in image quality are expected from these systems.

In order to address these topics, the Monte Carlo code known as “MCMIS” (**M**onte **C**arlo for **M**ammography **I**mage **S**imulation), was used to simulate mammograms produced by a direct digital mammography system, specifically, the Fischer Senoscan<sup>TM</sup>. As mentioned previously, extensive benchmarking and testing of this code against computational results and even actual images of phantoms have been completed to demonstrate its ability to accurately simulate the output from the Senoscan<sup>TM</sup> (Peplow 1999). Use of the MCMIS code allowed us to vary several system parameters in order to address the issues at hand. The four parameters that were varied were microcalcification size and spacing, breast thickness, and detector pixel size. Each of these variations will be discussed in detail in the sections 2.3.1 to 2.3.3.

### 2.3.1 Microcalcification Phantom

In order to address the issues of image resolution and contrast, a computational microcalcification phantom that would allow convenient comparison of contrast and spatial

resolution between various detector pixel sizes was necessary. The phantom designed for this study makes use of both size and spacing variations to accommodate this requirement. For the MCMIS simulation, spheres of bone-mineral hydroxyapatite, a material similar in composition to the composition of microcalcifications, were used. Information on material composition for bone-mineral hydroxyapatite was taken from ICRU Report 46 (1992). The total dimensions of the phantom were approximately 1.6 cm x 1 cm x 0.04 cm. Figure 2.1 shows an enlarged view of the complete microcalcification phantom.

The spheres were arranged in pairs in a matrix-like grid. For this work, a cluster was considered to be a pair of microcalcifications. The spacing between the two spheres in each pair (from edge to edge) is varied from the top of the phantom to the bottom, starting with a 25  $\mu\text{m}$  space and ending with a 200  $\mu\text{m}$  space, in increments of 25  $\mu\text{m}$ . In each pair of microcalcifications, the left member's diameter was kept constant at 400  $\mu\text{m}$ , while the diameter of the microcalcification on the right was varied from 50  $\mu\text{m}$  to 400  $\mu\text{m}$ . The right-hand side microcalcification diameter was increased for each pair in increments of 50  $\mu\text{m}$  from left to right.

The 400  $\mu\text{m}$  microcalcifications on the left side of each microcalcification cluster were kept stationary in the x-direction for each column, and were spaced 1450  $\mu\text{m}$  from center to center in the y-direction. The spacing between columns was set at 2050  $\mu\text{m}$ . This distance was measured from the centers of the left-hand side microcalcifications in each column to the centers of the left-hand side microcalcifications in the next column.

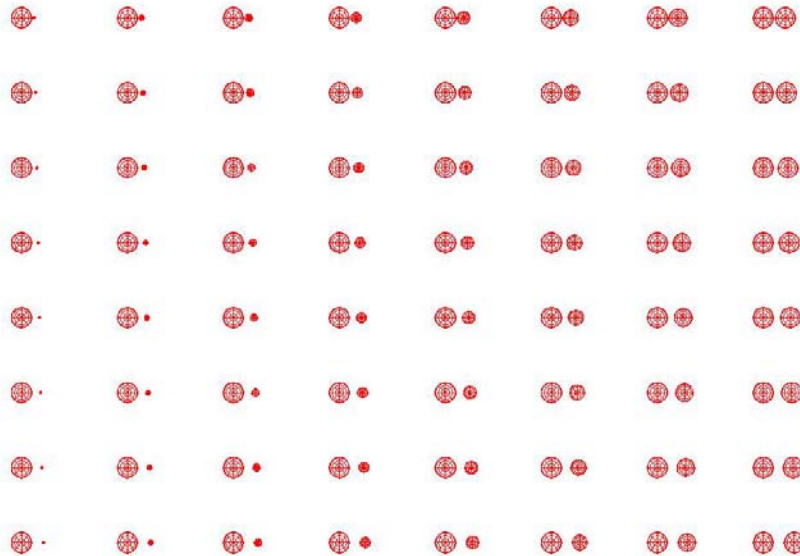


**Figure 2.1 Top view of microcalcification cluster phantom used in MCMIS simulations. The diameter of the largest microcalcifications is 400  $\mu\text{m}$ , while the diameter of the smallest is 50  $\mu\text{m}$ . The smallest spacing between a microcalcification cluster is 25  $\mu\text{m}$  (top row), while the largest is 200  $\mu\text{m}$  (bottom row).**

The geometry input data used for the phantom and all other objects in the simulation are included in the `geom.inp` file for the MCMIS code. This file and all other input files for the MCMIS code are included at the end of this work in Appendix I. A brief description of how MCMIS reads each file is also included in Appendix I.

This microcalcification phantom allowed us to address both detector resolution and contrast. The spacing difference between microcalcifications in each cluster allowed us to determine the minimum spacing required for resolving both objects in the cluster, rather than seeing a single image that represents both objects. The latter can occur because of two

issues. First, image smearing caused by the system MTF can cause two objects sufficiently close enough to “run together” and appear as a single object. Secondly, objects that are smaller than the dimensions of a single pixel and are significantly close to a larger object will not appear separated on the image. This is because the larger object will overwhelm the smaller object’s contribution to the image, and therefore the two will not be seen as individual objects on the mammogram.

### 2.3.2 Breast Phantom

The second parameter that was varied in this work was breast thickness. The purpose for varying this parameter was to determine whether or not a significant amount of image quality might be lost in imaging thicker breasts. Also, if image quality can be maintained using newer detectors with a decrease in breast compression, it is possible that more women would find breast screening a less painful experience, and therefore be more willing to participate in mammographic screening on a regular basis.

The breast phantom in this study was composed of two nested regions of 50/50 glandular/fatty tissue. Figure 2.2 shows in detail the 4 different breast thickness models. The geometry used for both regions was a curved plate, with the smaller of the two regions nested inside of the larger. The outer region, which extends 0.1 cm around the inner region, represents the skin layer, while the inside of the smaller region represents the breast tissue. The length of the breast extending from the chest wall was 15 cm, while the width of the breast along the chest wall was 12 cm. Four breast thicknesses were used in the simulations; 4, 5, 6, and 7 cm. The microcalcification phantom was then centered inside of the breast region as shown in Figure 2.2.

It should be noted that the microcalcification phantom is located in each breast phantom and is centered in the x- and y-directions for each breast. However, it is only centered in the z-direction for the 4 cm breast thickness. The position in the z-direction was then kept equal to the position in the 4 cm breast. The reason for keeping the z-axis position constant for all breast thicknesses was to limit variability in geometry that may result in image effects. These effects were discovered early on in running simulations when the microcalcification phantom was centered for every breast thickness. The resulting images for the 5, 6, and 7 cm breast thickness had phantoms that shifted location from the original location in the image. Therefore, to eliminate this shift as an additional variable in image analysis, the z-axis position was kept constant for all variations of breast thickness.

Despite the fact that the edges of this particular phantom are not curved as they might be in an actual breast imaging geometry, and no nipple is present, these phantoms being small are assumed to be an accurate enough representation of a breast for the simulations. Since the goals of this study focus on the microcalcification phantom, edge effects for the breast were considered unimportant. The phantom is located sufficiently far away from the edges of all of the phantoms to be unaffected by edge effects of the breast.

### 2.3.3 Source and Detector Set-Up

The final parameter varied in the simulations for this study was the detector pixel size. The basic source/detector set-up used for all simulations was the same as that of the Senoscan™. In this study, the basic source/detector arrangement used was a rastered point source over a curved detector in order to simulate as closely as possible the Fischer Senoscan™ system, which is shown schematically in Figure 2.3 (Peplow 1999). The nipple is shown only for orienting the reader to the geometry of the system. For the source, a

polyenergetic, divergent point source was used in the simulation. The source was located 63.8 cm above the detector grid in the plane of the chest wall, as demonstrated in Figure 2.3. The source sweeps out an 18 cm arc in the curved (scanning) direction and is 18 cm long in the y-direction. The slot width for the source collimator is 1.3 cm in the scan direction.

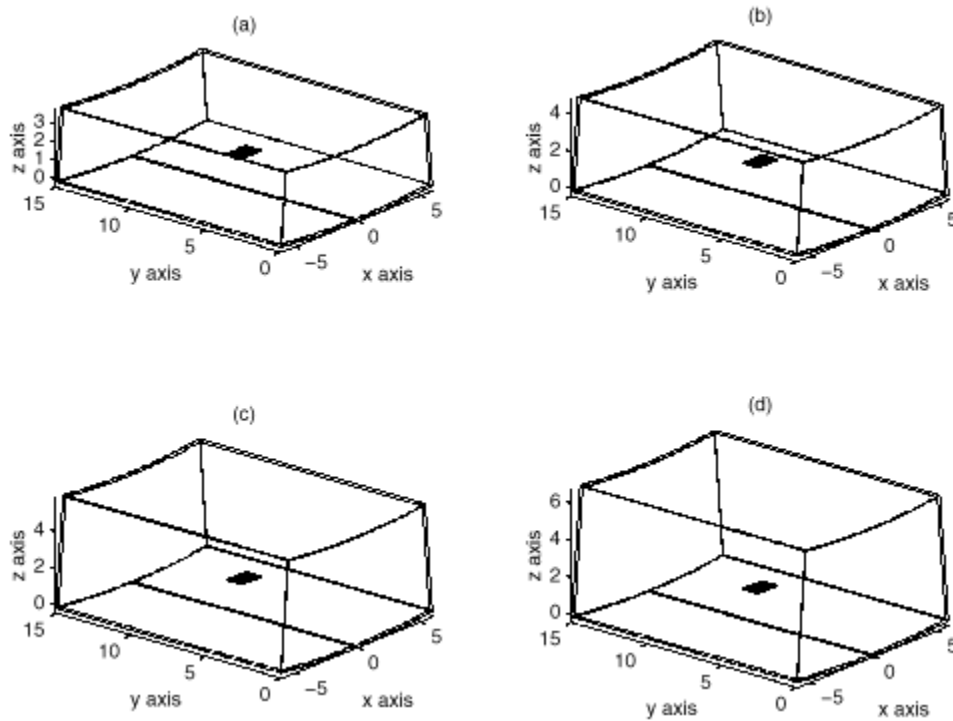


**Figure 2.2 Side view of breast phantoms used in the MCMIS simulations with microcalcification phantom shown in each breast for (a) 4 cm, (b) 5 cm, (c) 6 cm, and (d) 7 cm breast thicknesses.**

The detector chosen for the simulation was cylindrical wall detector with an active width of 1 cm in the scan direction, which is shaped like a curved plate in order to conform to

the shape of the lower support of the mammography system. The material properties used for the detector were equivalent to those used in the Fischer Senoscan™ mammography system. The phosphor has a material density thickness  $0.06765 \text{ g/cm}^2$  and is  $0.015 \text{ cm}$  thick.

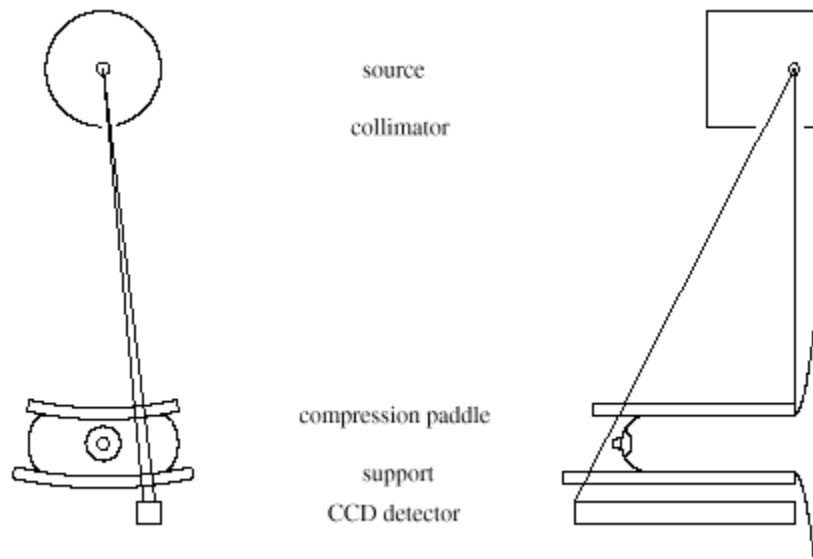


**Figure 2.3** The Fischer Senoscan™ scanning slot digital mammography unit. The anode and CCD detector array move together scanning the breast with a well-collimated fan beam. (Not to scale)

Three different detector grid sizes were used for the simulations performed. They were  $100$ ,  $50$ , and  $25 \mu\text{m}$  pixel detectors. The total grid size for the  $100 \mu\text{m}$  detector was  $400 \times 1500$  pixels, giving a total detector area of  $60 \text{ cm}^2$ . The total grid size of the  $50 \mu\text{m}$  detector was  $800 \times 800$ , giving a total detector area of  $16 \text{ cm}^2$ . The total grid size for the  $25 \mu\text{m}$  detector was  $1000 \times 1000$  pixels, giving a total detector area of  $6.25 \text{ cm}^2$ . Even though the detector dimensions differed for each detector pixel size, the detector position was always

chosen so that the microcalcification phantom would lie at the exact center of the image produced after the MCMIS simulation.

The reason for choosing these three detector sizes was to emulate as closely as possible digital mammography modalities that are currently available or that are undergoing testing. While many digital mammography systems still use the 100  $\mu\text{m}$  pixel detectors, more recent modalities, such as the Senoscan<sup>TM</sup>, are also capable of using detector sizes of 50  $\mu\text{m}$ , and are expected to replace current clinical mammography systems. Even more recent advances have produced detectors with even smaller pixel sizes than the Fischer system on the order of 25  $\mu\text{m}$ , and may prove more useful than detectors used in systems such as the Senoscan<sup>TM</sup>. This study made use of these various pixel sizes in order to demonstrate not only which detector size might prove more useful to the radiologist, but also how much better the newest detectors may prove to be.

#### 2.3.4 Other MCMIS Parameters

In total, a user must produce 4 input files for each run of the MCMIS code. These four files are called `geom.inp`, `mater.inp`, `mc.inp`, and `sode.inp`. The first of these files, `geom.inp`, is the input file from which the code gathers all information on the geometry of the problem being addressed. This file includes the information on the microcalcifications (section 2.3.1), the breast region (2.3.2), as well as any other regions that are included in the problem. For the cases run for this particular study, three additional regions are included in this file in addition to those already discussed in detail. These are the compression paddle, the breast support shelf, and wedge of air surrounding all other regions in the problem. The air wedge is included so that scattering effects can be included in simulations.

The file mater.inp is used to dictate to MCMIS the materials to be used for the various regions in a simulation run. This file indicates which MCMIS material libraries are to be used for a given simulation, as well as which materials are to be used from the libraries chosen. MCMIS has two material form factor libraries from which to choose form factors; an atomic form factor library and a molecular form factor library. The molecular form factor library was created from actual measured data (Peplow and Verghese, 1998).

Mc.inp is the file in which all pertinent Monte Carlo information is stored. This file includes information on the number of histories to be used in a simulation. The first of these is the number of particle histories per pixel that will be used, while the second tells MCMIS how many outer loops should be run. Each time an outer loop is finished, information gathered so far is dumped to a file. This allows the user to view the image while the code is still running in order to determine whether or not any problems are occurring during the simulation. This then allows the user to stop a faulty simulation without having to wait for the code to run to completion. Also, the user enters the Russian Roulette minimum weight to be used during the simulation in this file. This number dictates the minimum weight that a particle will have during a simulation before Russian Roulette is played on the particle to see if it continues its flight or dies. The weight chosen for this simulation is  $1.0 \times 10^{-4}$ . Finally, four other options can be turned on or off by the user in this file through use of Fortran logical statements. The first logical statement allows a user to choose whether X-ray fluorescence will contribute significantly to a simulation or not. This option was not used in any of the simulations presented in this work since implicit capture prevents simulation of photoelectric events. The last three options allow the user to choose which variance reduction methods will be used during the simulation. Variance reduction methods are used

to reduce the number of particle histories necessary to produce statistically valid results for a simulation. The variance reduction methods available are last flight estimator, point detectors, and implicit capture. All three variance reduction methods were used in all simulations completed for this work.

A more detailed description of the input files as well as examples of each file used in simulations will be included in Appendix I of this work.

## Chapter 3

# Image Production and Analysis

This chapter describes the basic techniques used in the image simulation process. First, a description of how a simulated image is produced using Matlab™ will be given. A description of the image analysis tools developed and used will complete this chapter.

### 3.1 Image Production

The MCMIS code itself does not create the actual simulated image that we desire, but instead produces several output files that contain information that would be gathered by the detector in a clinical setting. These must be processed by another program that creates the simulated image. For this work, Matlab™ was used for all image processing.

A single MCMIS run produces the results in the form of several output files for a monoenergetic source. These files include the fine mesh image, or “flash” image, from unscattered photons, a coarse mesh image from the contribution of scattered photons, and the statistical error for both. Since a single MCMIS run only produces these data for a single source energy, a series of MCMIS runs must be completed for each energy within the source spectrum. For this study, the source spectrum was chosen to be that of a tungsten target with a 500  $\mu\text{m}$  Al filter with a 40 kVp potential. Figure 3.1 gives the flux spectrum for such a source and is taken from the work of Boone *et al* (1997) and was used by Peplow (1999). As can be seen in the figure, contributions to the flux are only significant for this spectrum

between 5 and 40 keV. Therefore, only energies ranging from 5 to 40 keV were used in simulating the images in 1 keV increments.

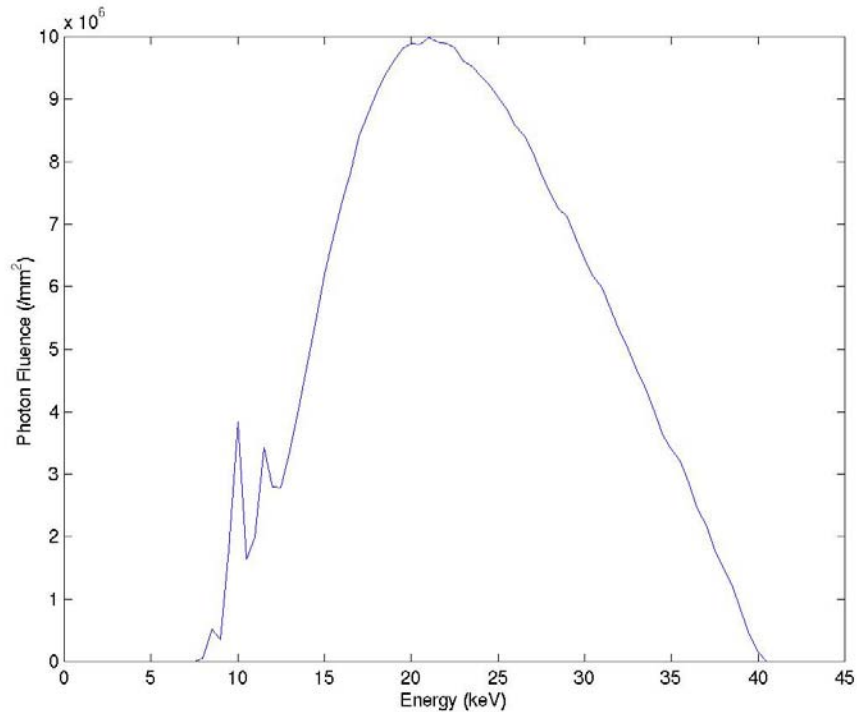


**Figure 3.1 Source spectrum used to simulate images produced by the Fischer Senoscan system. The target material for this source is tungsten with a 500  $\mu\text{m}$  aluminum filter (Peplow 1999).**

After all MCMIS runs have been completed, a Matlab™ routine is used to perform four major steps in the image production process. These four components to the production of a final image are (1) weighting contributions to the image from each energy of the source based on the source spectrum for both the flash and scatter images, (2) adding together the

properly weighted contributions into a single image, (3) interpolating the total scatter map and adding it to the unscattered image, and (4) smearing the combined image with the system MTF. These four steps will be discussed in the following sections 3.1.1 to 3.1.4. Appendix II includes the Matlab™ script used to produce the images for each case, as well as the algorithm used to develop the image production routine. It should be noted that an additional 5<sup>th</sup> step can also be included in the image processing in which white-line noise is added to the image. This step is included in the image processing routine in Appendix II, but was not included in the analysis of images in this work. For this work, only the ideal case in which there is no additional detector noise was necessary.

### 3.1.1 Weighting Contributions from Monoenergetic MCMIS Runs

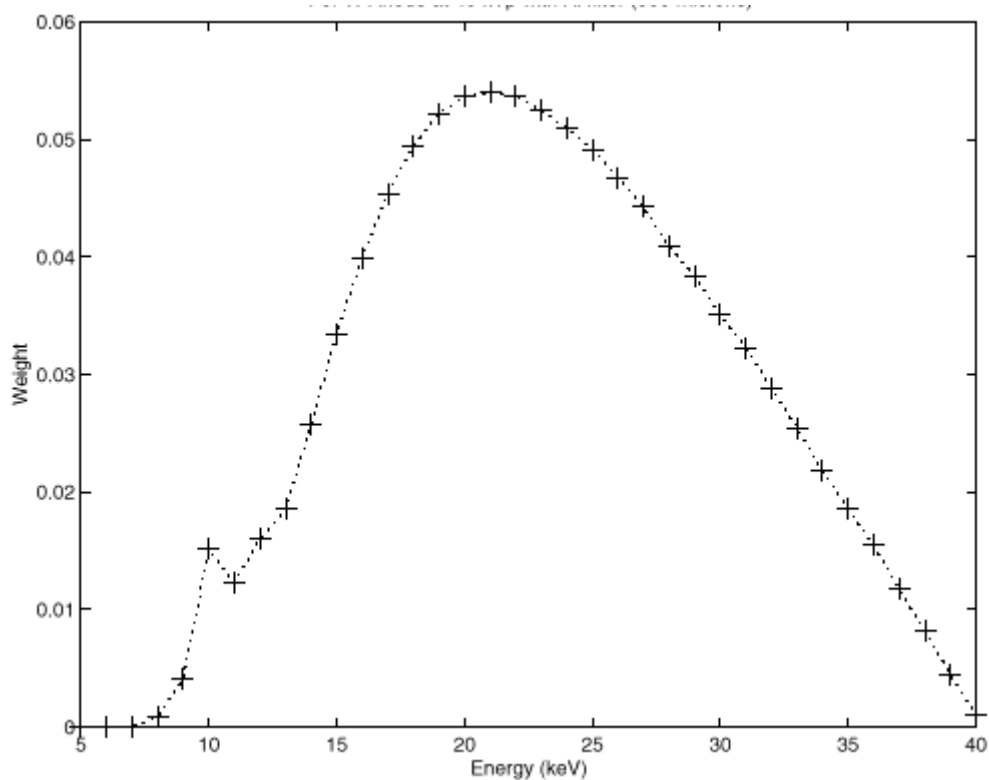
For each mammography system, various tube/filter combinations are used to produce X-rays. For this study, the Senoscan™ is the system of interest, so the parameters chosen for image processing were chosen to match the characteristics of this system. A characteristic X-ray spectrum will result from the parameters chosen, and must be included in the processing of the raw MC monoenergetic data. The first step in the image production process is weighting the output from each MCMIS run according to the spectrum data for the device that is being used. The weights are calculated using a C code developed by Boone *et al* (1997) from the spectrum shown in Figure 3.1.

Figure 3.2 shows a plot of the weights used for this work. The source energies used in the MCMIS runs are indicated by the “+”s in the figure.

### 3.1.2 Addition of Weighted Images

Since MCMIS produces a separate set of detector tallies for each energy in the spectrum, to produce a single, complete image, one must next add up all of the weighted

tallies. For this work, this was done for two different cases of images. The first case is that which contains the contribution to the image from exponential photon attenuation, or the “flash” image, and the contribution to the image from scattered photons. The contribution from unscattered and scattered photons is discussed more thoroughly in section 3.1.3. The second case contains both of these contributions as well, but also includes various effects on the image that are intrinsic to the mammography system, also known as the modulation transfer function, or MTF for short. The effects of the MTF are discussed in more detail in section 3.1.4.



**Figure 3.2 Weight vs. MC Energy.** These weights were determined using the source spectrum given in Figure 3.1. “+”s indicate the source energies used for each monoenergetic MCMIS run.

### 3.1.3 Scatter Map Interpolation

MCMIS produces three separate files for the unscattered and scattered contributions to the image for each monoenergetic run. Since the flash image is produced without the use of Monte Carlo, this image is produced relatively quickly, even for extremely large numbers of detector pixels. However, production of the scattered contribution does rely on the use of Monte Carlo, and therefore would take a long time to run a single monoenergetic case for the large number of pixels that would be required to span the entire breast region used in this work. Therefore, the scattered contribution is produced using a detector grid size smaller than that used to produce the flash portion of the image in addition to a larger pixel size. Using the smaller detector grid allows us to focus just on the region of the breast including the microcalcification phantom. When processing the files to create a complete image, though, all contributions must have matching pixel size. Therefore, the scattered contribution must be resized into a grid of equal size to the flash contribution. This is done using an interpolation routine.

### 3.1.4 Smearing the Image with the System MTF

The final step in producing a complete image is “smearing” the image with the system MTF. This process is known as smearing because in an image where the MTF has not been included, the edges of objects appear very sharp, and it is relatively easy to distinguish boundaries between objects that are within the resolution capabilities of the detector. After application of the MTF, though, the edges of objects appear to spread out and run together with nearby objects, producing a smooth, continuous image. Figure 3.3 demonstrates this effect on a single microcalcification cluster.

## 3.2 Production and Implementation of Analysis Tools

After producing a complete image, analysis of the images can be performed. Before analyzing the images, however, a set of tools had to be developed in order to analyze the image characteristics of interest. Matlab™ was again the program of choice for analysis of the images, so several scripts were developed for this purpose. These scripts, as well as the algorithms used to develop them, may also be found in Appendix II.

Both the smeared and unsmeared images produced for each set of detector and breast conditions were used in the analysis. The unsmeared images are considered “ideal” images for each detector since this type of image excludes any smearing inherent to the mammography system. The smeared images are considered more realistic, since these are more similar to what one would see in an actual mammogram. However, it should be noted that even these images are incomplete in that they do not include contributions from noise, and are free of any other heterogeneities that can be commonly distinguished in mammograms, such as mammary ducts.

The first analysis tool developed was one that would allow us to gain some insight into how well the detector was able to resolve microcalcifications. Resolution is defined for this work as *how many individual microcalcifications can be seen* in each image. The script written for this part of the work tallied the total number of calcifications detected. The method used to calculate the number of visible calcifications is explained in more detail in section 3.2.1, and also in Appendix II. Using the methods set forth in these sections, a fraction of microcalcifications detected was calculated for each image. A detector with a fraction close to one would indicate a very good resolution for that particular detector.

The second analysis tool discussed in this section is a Matlab™ script used to determine contrast for each image. Contrast is here *a measure of how well microcalcifications can be distinguished from surrounding breast material* in each image. The script developed for this section of code returns a value that allows one to determine the difference in intensity of a region that is inside a microcalcification, and a region that is clearly outside a microcalcification. A larger value for contrast denotes greater ease in determining what is and what is not a microcalcification.

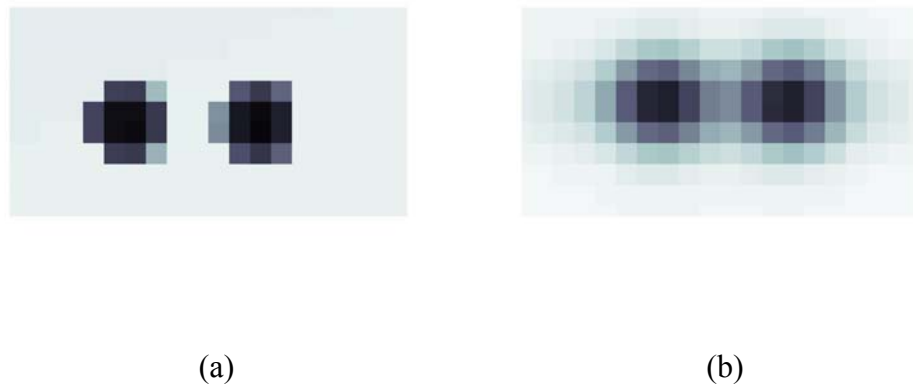


**Figure 3.3** A microcalcification pair from the image produced using a 100- $\mu\text{m}$  pixel detector and a 4-cm breast thickness. Figure (a) is the cluster seen without smearing from the MTF. Figure (b) includes MTF smearing. The microcalcifications shown are both 400  $\mu\text{m}$  in diameter.

### 3.2.1 Calculation of Resolution

Determining resolution of an image consists of five steps, which are repeated for each row of microcalcifications in a single image. The first step in this process is to determine a region of interest (ROI) around a single row of microcalcifications in a given image. This

region should be carefully chosen so that only contributions from a single row are included in the image data matrix.

Next, the user should choose a threshold pixel value. The purpose of this threshold value is to determine whether or not a given pixel's value lies within or outside of a microcalcification. Choosing this value can be rather tricky and it should not be chosen arbitrarily. An easy place to start with guesses for the optimal threshold is the average pixel value within the ROI. For this work, the average value for each ROI was chosen as a reference point then fractions of the average ranging from 0.75 to 1.01 were used as threshold values. This range was chosen by extensive trials. A range of values was used because there is significant sensitivity to where one chooses the threshold, and would become even more so if quantum mottle was included in the image. The range of values, therefore, allows us to see which threshold value allows the highest number of microcalcifications to be counted. Figures 3.4 and 3.5 demonstrate the thresholds chosen for a given row of microcalcifications. One can see from these figures that if a value for the threshold is chosen too high or too low, microcalcifications that are visible in the image may be counted as unseen.

The third step in the process of calculating image resolution is to step through the ROI data matrix one column at a time. For each column, each element should be compared to the threshold in order to determine if one or more of the elements is less than the threshold value. If a single pixel in the column exceeds the threshold, the column has part of a microcalcification in it, and is assigned the value of 1. Otherwise, the column contains no contribution from microcalcifications, and is assigned a value of 0. This produces a row

vector of 1s and 0s indicating which columns of the ROI have contributions from a microcalcification and those that have only breast material information.

Next, we wish to count how many microcalcifications we have actually discovered in the original ROI. We can accomplish this by subtracting the  $i^{\text{th}}$  element of this row vector from the  $i+1^{\text{st}}$  element. Subtracting the elements in this way for the length of the row vector produces another row vector one element shorter than the previous row vector. This row vector will now contain  $-1$ s,  $0$ s, and  $1$ s. Each of these values signifies a certain characteristic of the image. A value of  $-1$  indicates that a sharp decrease in the horizontal (x-axis) slope of the image has occurred. This equates to the beginning of a microcalcification region. A value of  $0$  denotes a region in which the slope is not rapidly changing in the horizontal direction. A value of  $0$  therefore equates to a region either inside a microcalcification or region of breast material. Finally, a value of  $1$  indicates that a sharp increase in the horizontal slope of the image has occurred. This equates to the end of a microcalcification region.

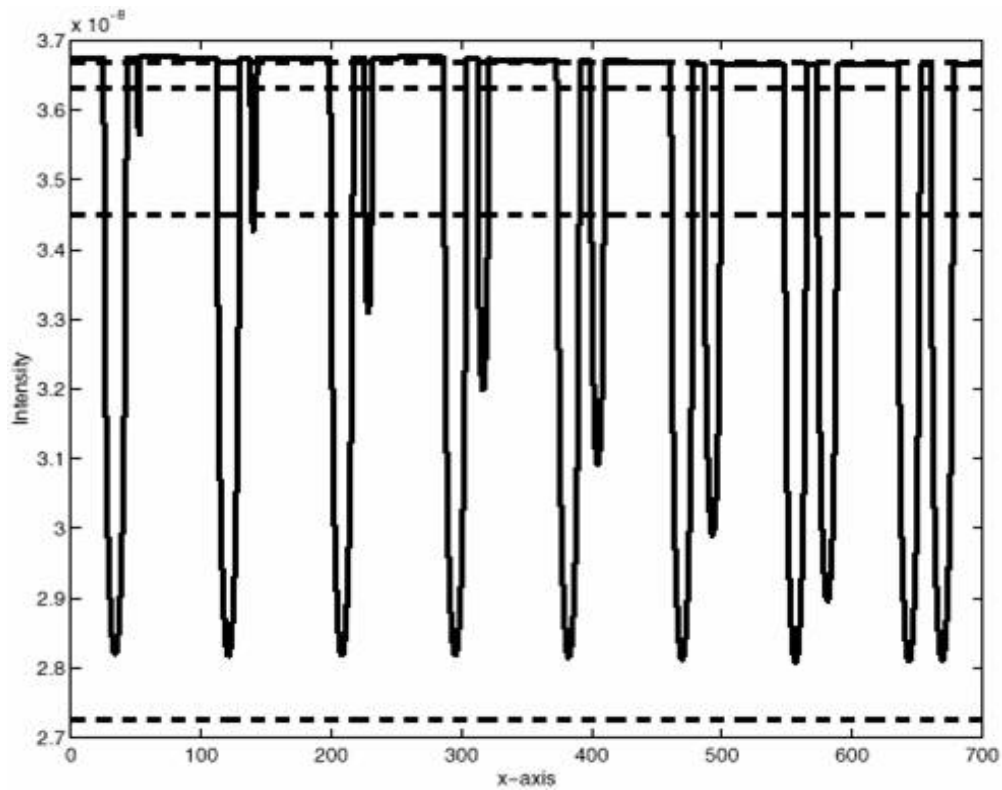
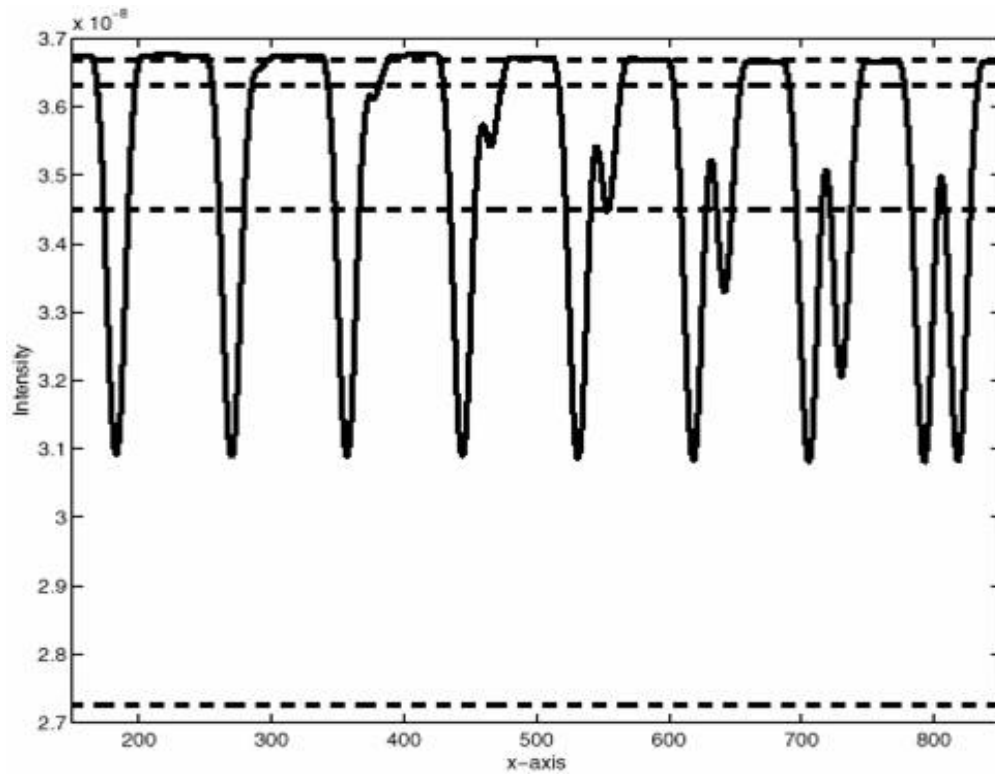
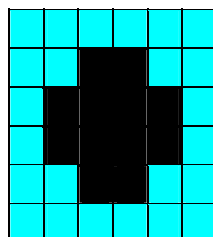


Figure 3.4 Pixel values for a single row of pixels in the center of a row of microcalcifications (A “line scan”) in an unsmearred image. The line scan shown is for the center row of pixels in an image of a 4 cm breast on a 25  $\mu\text{m}$  pixel detector. The spacing between microcalcification pairs is 200  $\mu\text{m}$ . The dashed lines indicate various values used as a threshold for determining where microcalcifications lie. The four thresholds shown are from top to bottom 1.01, 0.99, 0.95, and 0.75 times the average pixel value for the region of interest around the microcalcification row chosen.



**Figure 3.5** Line scan for a smeared image. The line scan shown is for the center row of pixels in an image of a 4 cm breast on a 25  $\mu\text{m}$  pixel detector. The spacing between microcalcification pairs is 200  $\mu\text{m}$ . The dashed lines indicate various values used as a threshold for determining where microcalcifications lie. The four thresholds shown are from top to bottom 1.01, 0.99, 0.95, and 0.75 times the average pixel value for the region of interest around the microcalcification row chosen.



(a)

0.6	0.6	0.6	0.6	0.6	0.6
0.6	0.6	0.1	0.1	0.6	0.6
0.6	0.1	0.1	0.1	0.1	0.6
0.6	0.1	0.1	0.1	0.1	0.6
0.6	0.6	0.1	0.1	0.6	0.6
0.6	0.6	0.6	0.6	0.6	0.6

(b)

0	1	1	1	1	0
---	---	---	---	---	---

(c)

	-1	0	0	0	1
--	----	---	---	---	---

(d)

Figure 3.6 Three steps used to determine area in which microcalcification is located. The image in (a) is a hypothetical microcalcification. The image in (b) is the matrix of tally values for each pixel in the image. Note that a value of 0.1 indicates a pixel located within a microcalcification, and 0.6 indicates a pixel outside of the microcalcification. The row of values in (c) is the row vector created by searching through each column vector of (b) for pixels inside a microcalcification. Note that the four innermost columns of (b) have been indicated to contain microcalcification contributions. The row of values in (d) is the difference of values in (c) going from left to right and indicates a change in slope occurring between the first and second column of pixels, as well as between the fifth and sixth columns. This indicates that a microcalcification is located in columns 2 through 5.

### 3.2.2 Calculation of Contrast

Calculating contrast is a bit less complicated than the process used to determine resolution, but also utilizes the user-defined threshold to determine which pixels will be considered inside a microcalcification. In order to calculate contrast, however, a region containing the entire phantom is used as the ROI, rather than just a single row of microcalcifications at a time. The ROI for contrast calculation was chosen to be 1.2 mm around the outside edge of the microcalcification phantom.

The definition used for contrast in this work is

$$C = \frac{|A_{in} - A_{out}|}{(A_{in} + A_{out})/2} \quad (1)$$

where  $A_{in}$  is the average pixel value for pixels inside of the microcalcifications,  $A_{out}$  is the average pixel value for pixels outside of the microcalcifications, and  $C$  is the contrast (Peplow, 1999). The range of values for  $C$  is between 0 and 2. Once the ROI has been determined for a region, a Matlab routine reads the matrix in for the ROI, and checks each element of the matrix against the user-defined threshold. If the value of an element is below the threshold value, it is added to the ‘inside’ tally. If the value of an element is above the threshold, it is added to the outside ‘tally’. Once all elements have been included in either the ‘inside’ or ‘outside’ tally, the average of each tally is determined. These are then used in conjunction with equation (1) to calculate the contrast for the entire image.

## Chapter 4

### Discussion of Image Analysis

In this chapter a discussion of the results of the analysis methods from chapter 3 used on the simulated data is included. This chapter has three sections. The first section gives the results for resolution as a function of detector pixel size. The second section shows the results for resolution as a function of breast thickness. The final section includes a discussion of results of varying breast thickness on image contrast.

#### 4.1 Resolution Effects

To begin this section, it should be recalled that images for four breast thicknesses with three different detector pixel sizes were simulated. This results in 12 images of the phantom produced by MCMIS. For each of these 12 images, both the unsmeared and smeared images were analyzed using the methods described in chapter three. Therefore, there are a total of 24 image sets to be analyzed. Discussing the analysis of every one of these images, including discussion on comparison and contrast to other images, would take an inordinate amount of time and space within this document. Therefore, for this and the following two sections, only four sets of images will be used in direct comparison in each section. For comparison of images with pixel size as the variable, only the 100- and 25- $\mu\text{m}$  images for the 4-cm breast thickness will be used. For those comparisons in which breast thickness is the variable, only the 4- and 7-cm images created with the 25- $\mu\text{m}$  pixel detector will be used. However, any plots included in each section will show general trends in data

for all of the images that will reinforce the comparisons made for the four images. The full set of results will be included in Appendix II for completeness.

The first part of our analysis will deal with what was defined as resolution in Chapter 3. Intuitively, one would expect that optimum resolution would be obtained in a mammogram for a minimum breast thickness, as well as minimum pixel dimensions. In this section of the analysis, we test this hypothesis by comparing breast images simulated with both varying pixel size and breast thickness over realistic ranges of dimensions for both. Two types of figures will be used to perform this task – (1) simulated images of the microcalcification phantom and (2) plots of maximum fraction of microcalcifications detected vs. breast thickness. Type (1) figures are used more as a qualitative comparison of cases, while type (2) figures are used to supplement the findings in the cluster images. As a point of clarification, the “maximum fraction of microcalcifications detected” means the largest value of microcalcifications detected for a given threshold. This threshold is not a constant for all images analyzed in this work, but was usually found to be between 95% and 100% of the ROI average pixel value for unsmeared images, and 90% to 95% of the average pixel value for images smeared with the MTF.

#### 4.1.1 Effect of Decreased Pixel Dimensions on Image Resolution

We begin this section with a comparison of the unsmeared images created using both a 25- $\mu\text{m}$  pixel detector and a 100- $\mu\text{m}$  pixel detector. These images can be seen in Figure 4.1. In both cases, the 4-cm thick breast geometry was used.

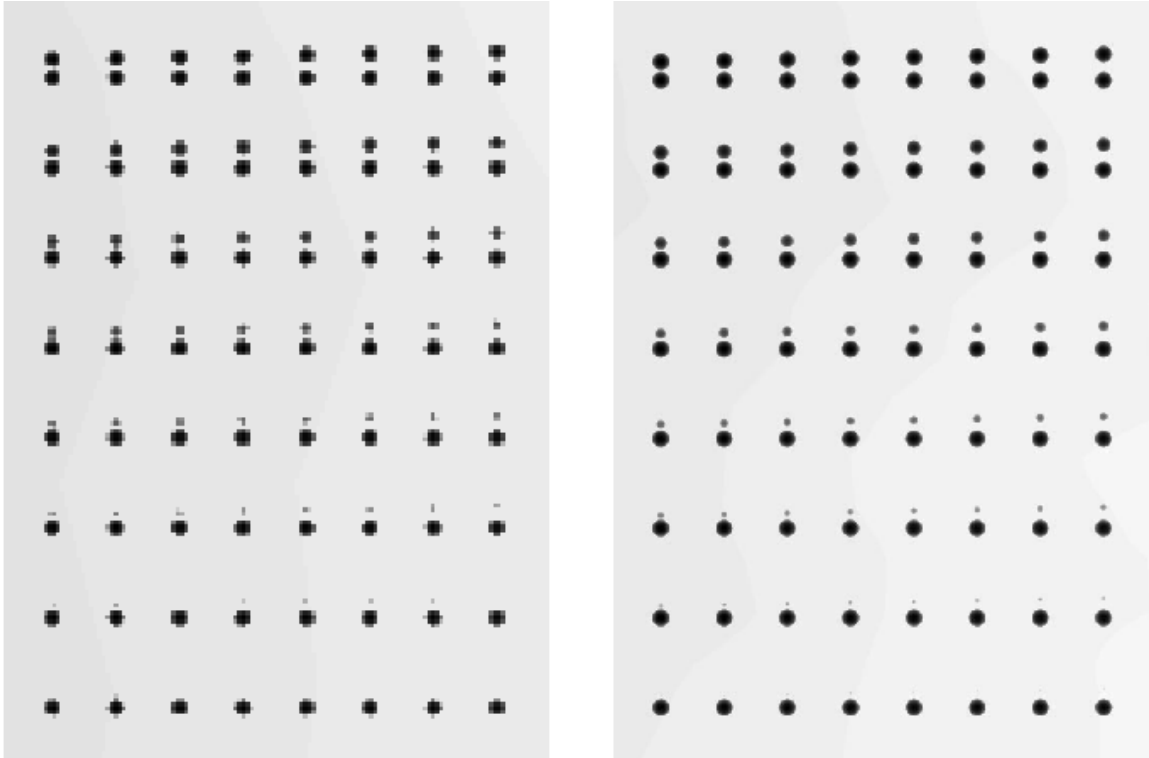


**Figure 4.1 Unsmearred images produced with a breast thickness of 4 cm. The image on the left was produced using a pixel size of 100  $\mu\text{m}$ . The image on the right was produced using a pixel size of 25  $\mu\text{m}$ .**

Right away we can see two main differences between the two images. The first is that the microcalcifications appear more round in the image created using the 25- $\mu\text{m}$  detector. The microcalcifications appear more rounded, as the 25  $\mu\text{m}$  pixel image allows better shape definition due to the larger number of pixels used to define a microcalcification. The second quality that is readily noticeable is that the 25- $\mu\text{m}$  image resolves more microcalcifications than the 100- $\mu\text{m}$  image. This initial finding bodes well for the smaller pixel size detectors in that resolution is better than the larger pixel size detector, as one might expect.

However, if we continue in our analysis by next viewing the same images that include the addition of the MTF, we see that our initial finding is not necessarily the right one.

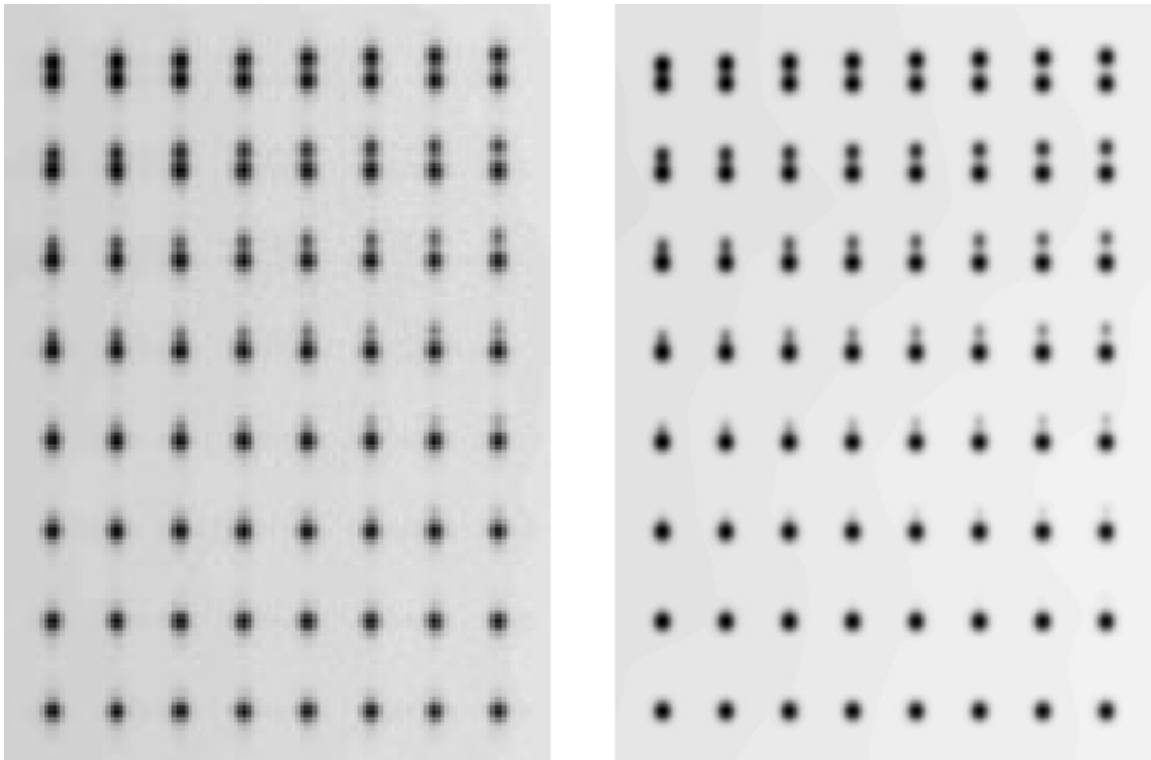


**Figure 4.2** Smeared images produced with a breast thickness of 4 cm. The image on the left was produced using a pixel size of 100  $\mu\text{m}$ . The image on the right was produced using a pixel size of 25  $\mu\text{m}$ .

In figure 4.2, we can see that once both of the images include effects from the detector MTFs, any increase in resolution originally seen in the 25- $\mu\text{m}$  image is reduced to the point that the images no longer appear to have any noticeable difference in their resolving capability.

We can see that is the general trend for all breast thicknesses over all detector pixel sizes if we look at figures 4.3 and 4.4. Figure 4.3 shows the maximum fraction of microcalcifications that can be viewed in each unsmeared image.

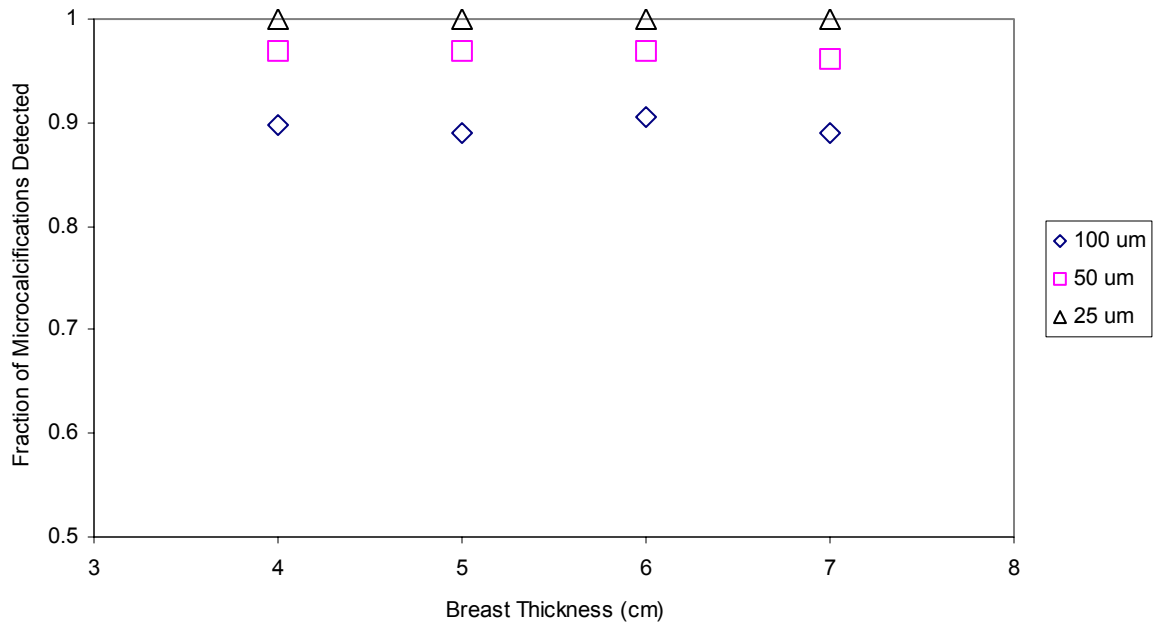


**Figure 4.3 Maximum fraction of microcalcifications visible versus breast thickness. These images were taken with 100, 50, and 25- $\mu\text{m}$  detectors, and did not include smearing with system MTF.**

As one might expect, for the 25- $\mu\text{m}$  images 100% of the microcalcifications were detected. The key point of interest in figure 4.3 is that the change in fraction detected when pixel size is varied is not very significant. Only an approximate 10% increase occurs between the 100- $\mu\text{m}$  and 25- $\mu\text{m}$  images for each breast thickness. This is significant, because it indicates that even for the ideal cases for these images, the improvement in resolution is quite small.

This is demonstrated to a greater extent when looking at Figure 4.4. In this image we can see that when detector MTF is included in the image production, not only is there a 30-35 % reduction in detector resolution for all detector types, but the difference in resolution between the detectors of varying pixel dimensions is diminished to about 5% when comparing the 25- and 100- $\mu\text{m}$  detectors. Thus, there is no significant change at all between the 50- and 100- $\mu\text{m}$  images.

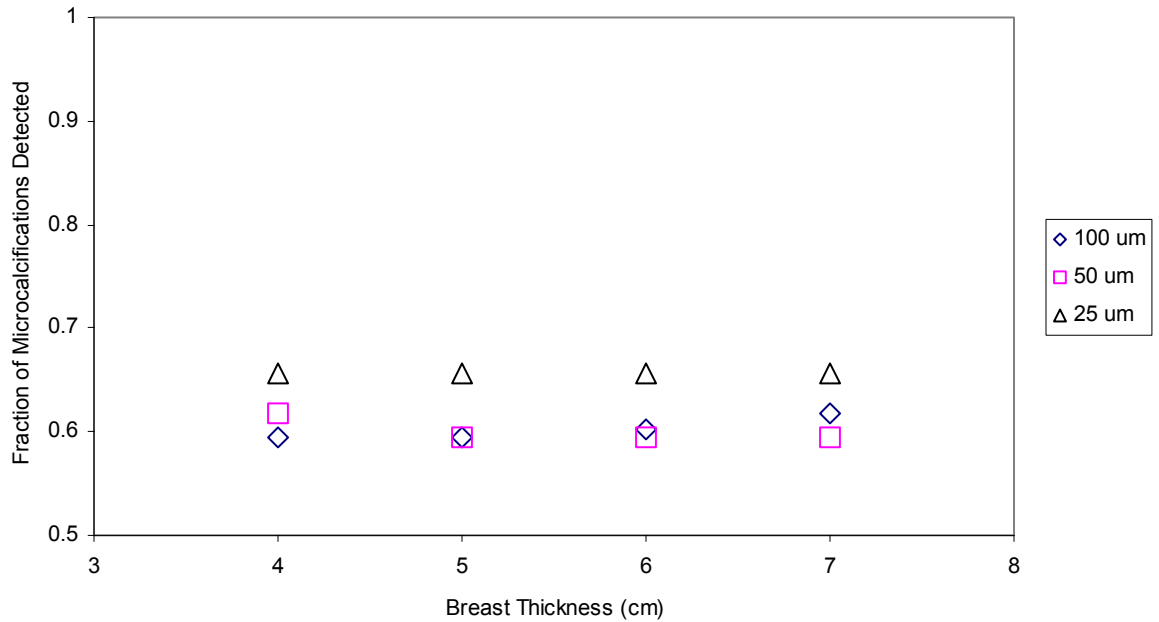


**Figure 4.4 Maximum fraction of microcalcifications visible versus breast thickness. These images were taken with 100, 50, and 25- $\mu\text{m}$  detectors, and include smearing with system MTF. Note that for the 5-cm breast thickness, the maximum value for the 50- $\mu\text{m}$  pixel detector and the 100- $\mu\text{m}$  detector overlap.**

One should recall also that for the smeared images, the MTF used for the images was the same. If the correct MTFs for the 100 and 25  $\mu\text{m}$  detectors were used, it is possible that the image quality could be degraded even further for the 100  $\mu\text{m}$  detector and less for the 25  $\mu\text{m}$  detector, though it is uncertain what the actual effects would be.

#### 4.1.2 Effect of Increased Breast Thickness on Image Resolution

Now we turn to comparison of images based on varied breast thickness. Figure 4.5 shows unsmeared images for both a 4-cm and 7-cm thick breast. The pixel size for these images is 25- $\mu\text{m}$ .

As one can see, both images contain the same number of resolved microcalcifications. However, as one would expect due to additional attenuation of photons in the breast material, the very smallest microcalcifications are a little more difficult to see in the 7-cm image when viewed at a higher magnification. However, this is more of a contrast issue, and therefore will be discussed more in depth in the next section. This trend also spans across the other two cases of varied breast thickness for each detector type. This is readily seen in Figure 4.3, where for each detector pixel size, the maximum fraction of microcalcifications detected remains relatively constant over the four cases for varied breast thickness.

Upon looking at the same images with the addition of the detector MTF in Figure 4.6, we see that this trend continues for the smeared image.

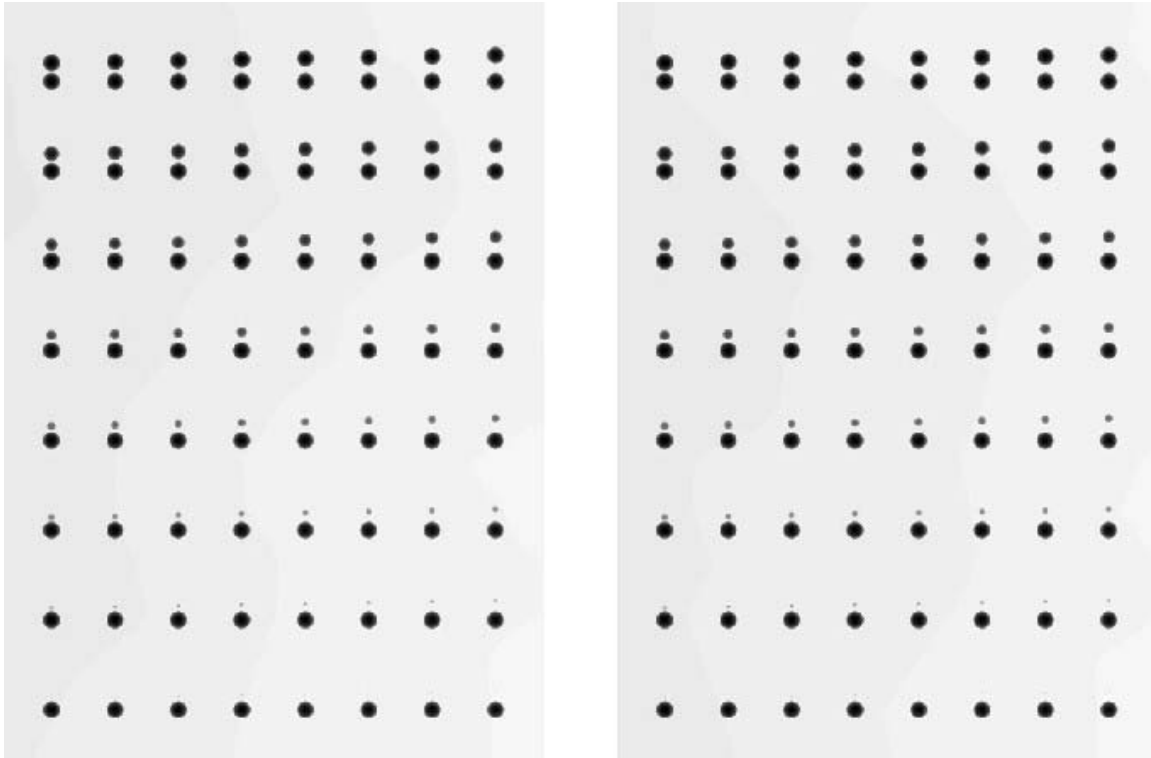


**Figure 4.5 Unsmearred images produced with a pixel size of 25  $\mu\text{m}$ . The image on the left was produced using a breast thickness of 4 cm. The image on the right was produced using a breast thickness of 7 cm.**

All microcalcifications seen in the 4-cm image are also seen in the 7-cm image, as well. Again, looking at Figure 4.4, we see that this is true for all breast thicknesses using the 25- $\mu\text{m}$  detector. However, we now see that there is a slight variation between breast thicknesses for both the 50- and 100- $\mu\text{m}$  cases. The variation occurs for only one of the 50- $\mu\text{m}$  images and for only two of the 100- $\mu\text{m}$  images, though, and is therefore more than likely due to MTF effects, rather than a global trend.

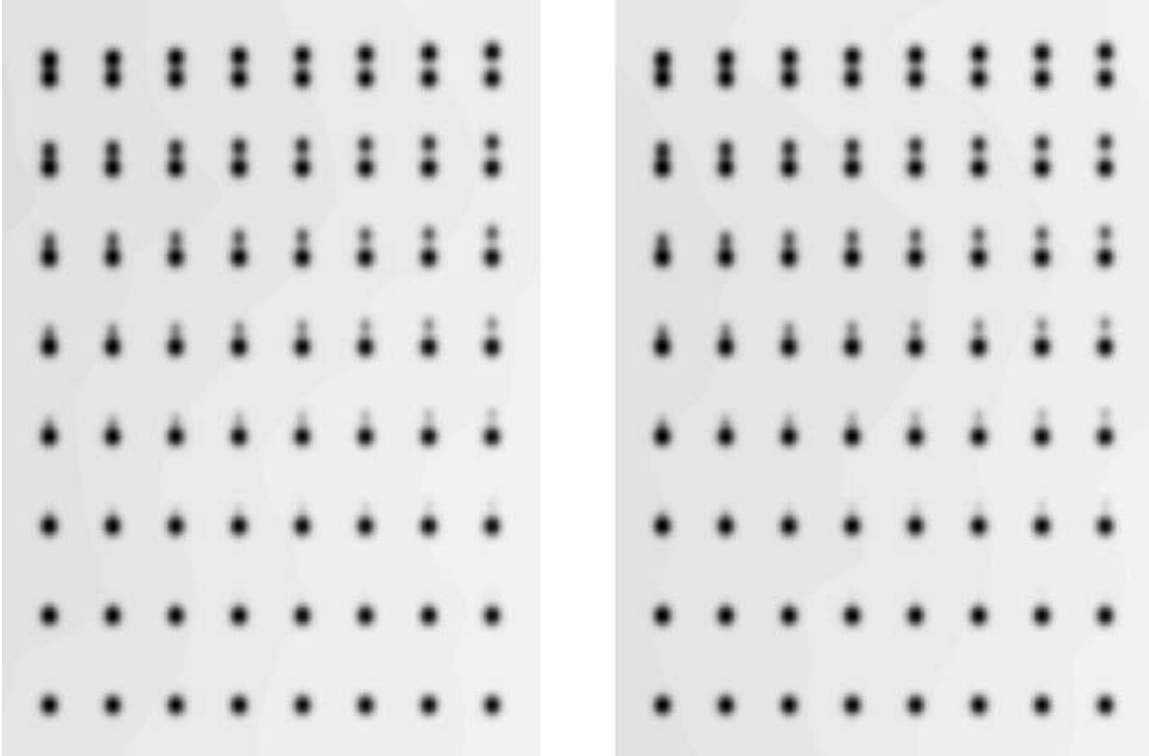


**Figure 4.6 Smearred images produced with a pixel size of 25  $\mu\text{m}$ . The image on the left was produced using a breast thickness of 4 cm. The image on the right was produced using a breast thickness of 7 cm.**

## 4.2 Contrast Effects

As with resolution, the variations in pixel size and breast thickness also affected the contrast of each of the images. For this work, rather than choosing the optimum value of contrast for analysis, the contrast at optimum resolution was used since we wish to see as many microcalcification pairs as possible. As discussed in Chapter three, the way in which contrast is defined results in a possible range of values for contrast between 0 and 2. For this particular study, we found that all of the contrast analysis done (i.e. plotting contrast as a function of threshold) resulted in a figure such as in Figure 4.7.

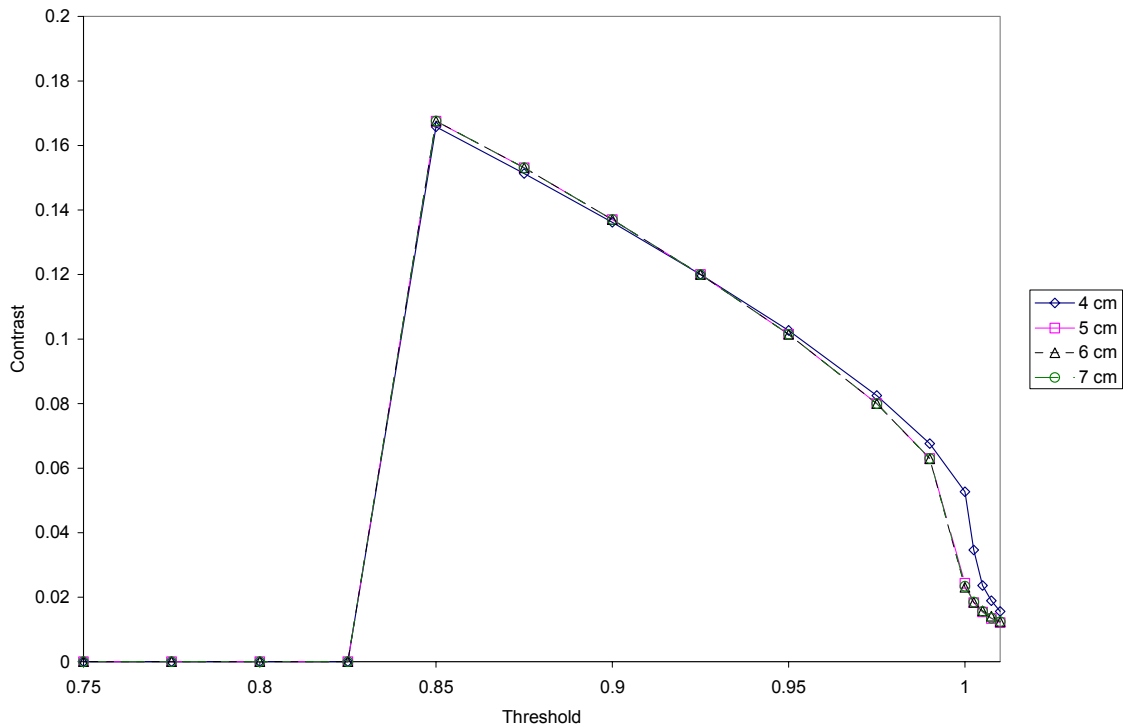


**Figure 4.7 Total image contrast data for each breast thickness for the 25- $\mu\text{m}$  pixel detector as a function of user defined threshold. Note that the data points not visible, especially for the 5- and 6-cm breast thickness, are overlapped by the data points for the 7cm breast thickness.**

If we look at the same such plot for each possible combination of breast thickness and pixel size, we will see that in general, the trend for these curves is that for threshold values below and up to a minimum threshold, the contrast is at a maximum of 0 (indicating that all pixels were chosen as breast material, and no microcalcifications are visible at that threshold). If we consider only the smeared images, this minimum appears to be relatively constant for a given detector pixel size, no matter the breast thickness. Table 4.1 lists the threshold for each pixel size.

Detector Pixel Size	Minimum Threshold
100 $\mu\text{m}$	0.9
50 $\mu\text{m}$	0.875*
25 $\mu\text{m}$	0.85

**Table 4.1 Minimum threshold values in the smeared images from each detector type used. Below this threshold, no microcalcifications are seen in any of the images for that detector, independent of breast thickness.**

**\*For the 50- $\mu\text{m}$  detector, the threshold for the 7-cm breast was 0.9.**

As also seen in Figure 4.7, above the minimum threshold, there is a sudden increase from zero to a region in which the contrast follows an almost linear trend, until it drops suddenly back towards zero when the threshold approaches 1. This also occurs in general for each detector type. Again, the contrast values chosen for analysis in this work are not those for the optimum value of contrast, but are instead determined at the threshold for which the resolution is also at a maximum. Figure 4.8 shows a graph of resolution versus the value for contrast determined at the same threshold.

As can be seen in the figure, most of the maximum values for resolution are focused in the plot between contrast values of 0.1 to 0.2, independent of detector pixel size. By choosing the point at which the optimum resolution occurs from a figure such as this, we can determine our optimum contrast for any combination of breast thickness and pixel size.

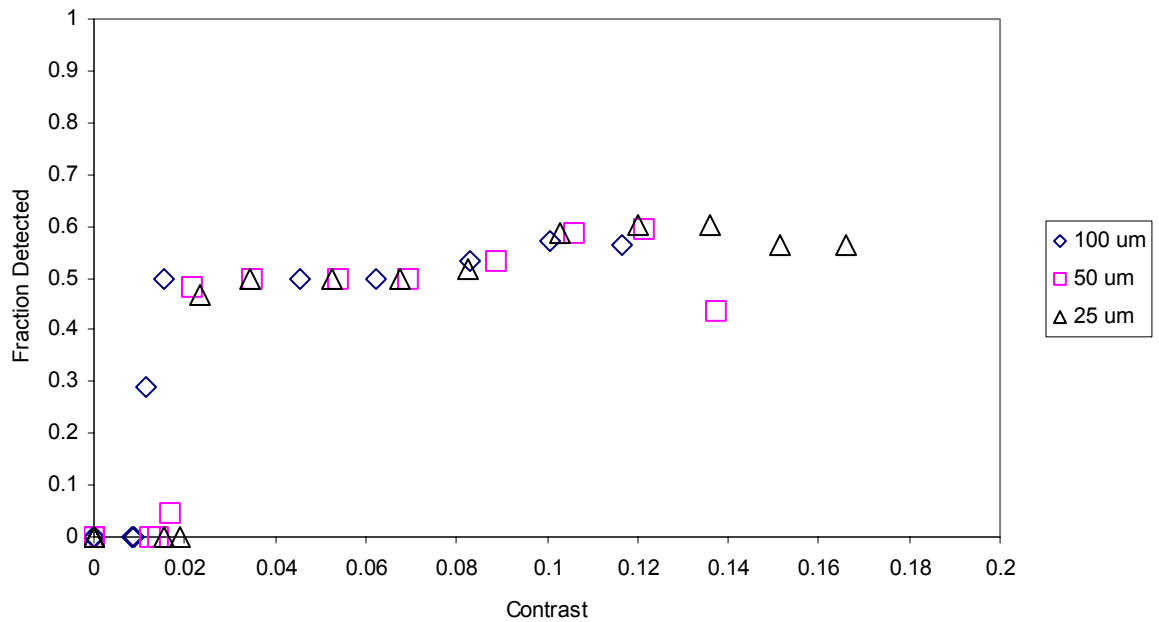


**Figure 4.8 Fraction of microcalcifications detected versus the contrast determined at a given threshold. Each point represents the contrast and resolution determined at a given threshold. Choosing the point at which the maximum resolution occurs gives us the optimum contrast for a given image.**

#### 4.2.1 Effect of Decreased Pixel Dimensions on Image Contrast

Unlike the previous sections that dealt with resolution effects, there is a large difference between the results found for the unsmearred and smearred images when comparing contrast for different detectors. This is readily evident from a comparison of Figures 4.9 and 4.10. In Figure 4.9, the results for optimum contrast as a function of pixel size are seen for images in which the detector MTF was not applied. There is no readily apparent trend in this data, and the reason for this is not entirely clear. The only trend that is seen across the board for each breast thickness is that contrast decreases for the 50- $\mu\text{m}$  images from the 25- $\mu\text{m}$  images, and then increases again for the 100- $\mu\text{m}$  images. However, there is no apparent

consistency between the different breast thicknesses that would indicate why this trend occurs.

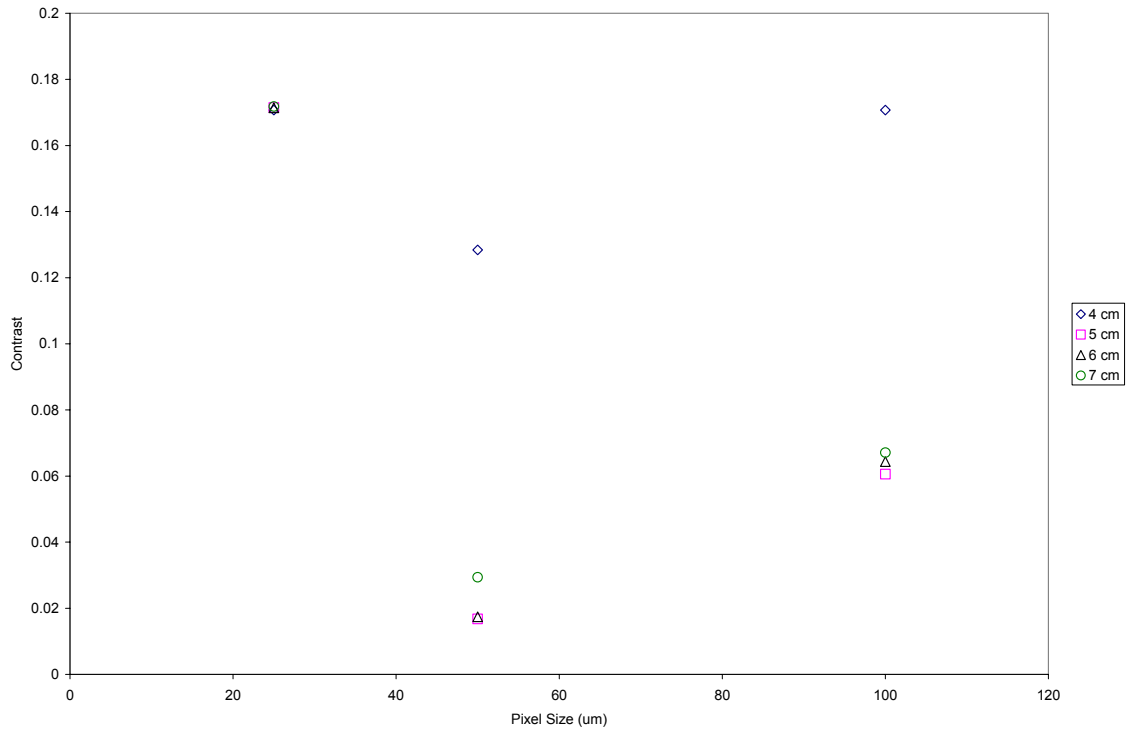


**Figure 4.9 Contrast versus detector pixel size for varied breast thickness. Data analyzed to produce these results were image data that does not include detector MTF. Note that for all values of breast thickness, the data overlaps for the 25- $\mu$ m pixel size detector.**

In figure 4.10, the same graph is shown for the data that includes the detector MTF. In this figure, there is a trend that is readily apparent. That is, as pixel size increases, contrast decreases for all variations of breast thickness. However, this decrease in contrast is not very pronounced. Even between the 100- $\mu$ m and 25- $\mu$ m images, the change in optimum contrast is only about 20% for every breast thickness.

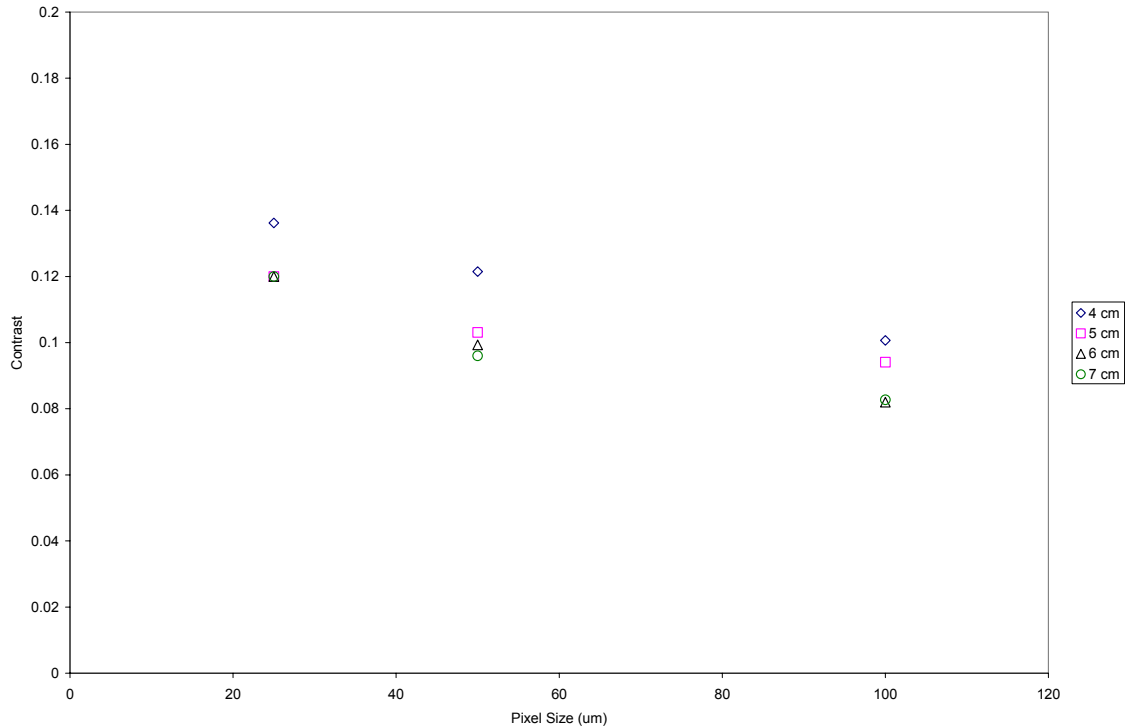


**Figure 4.10 Contrast versus detector pixel size for varied breast thickness. These data include the effects of the detector MTF. For the 5-, 6-, and 7-cm breast thickness images, the points overlap for the 25- $\mu$ m detector.**

#### 4.2.2 Effect of Increased Breast Thickness on Image Contrast

Finally, we look at the effects of increasing breast thickness on image contrast.

Figure 4.11 shows the results of varying breast thickness on optimum image contrast for images that did not include the MTF. As can be seen, the 50- and 100- $\mu$ m results, for the 4-cm thick breasts, contrast is at a peak, but drops off significantly for all other breast thicknesses. This is not the case, though, for the 25- $\mu$ m detector results. This suggests that, under optimum conditions, perhaps the 25- $\mu$ m detector does not have a significant drop in contrast until a much greater breast thickness is reached.

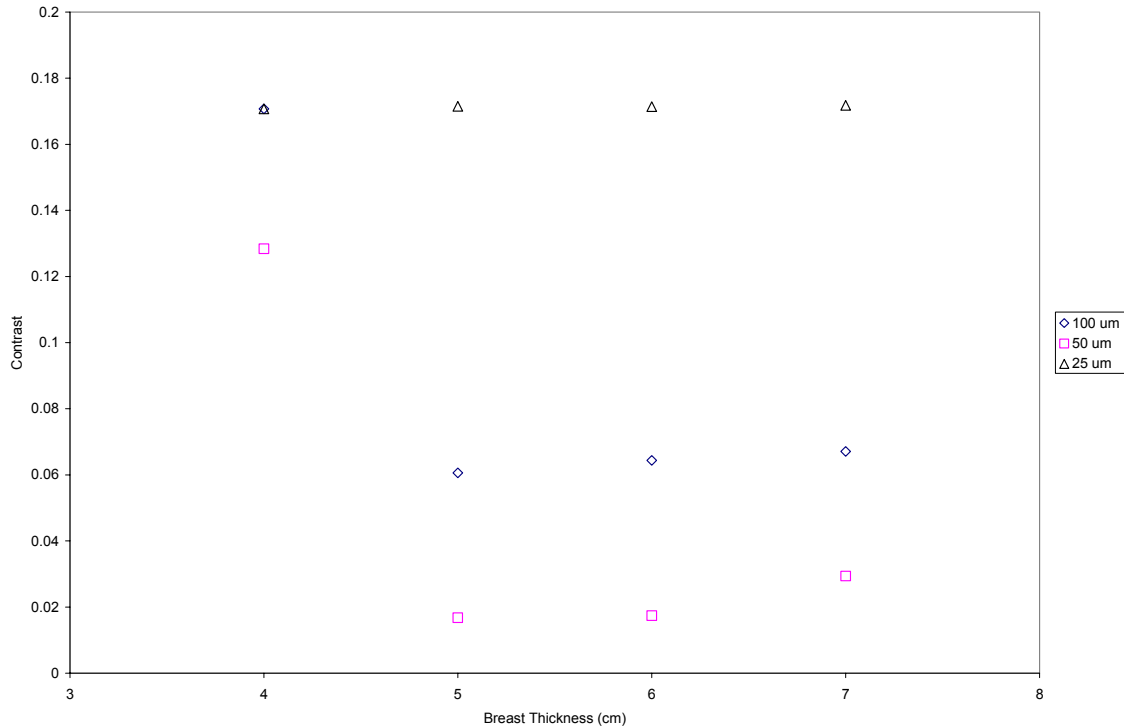


**Figure 4.11 Contrast versus breast thickness for three different detectors. The images used for this data did not include the use of the system MTF. For the 4-cm breast thickness, the data points overlap for the 25- and 100- $\mu\text{m}$  pixel detectors.**

However, if we turn our attention to Figure 4.12, we can see that when including the system MTF, an almost linear decrease in optimum contrast occurs for all the detector systems as breast thickness increases.

A point of interest here is that the drop in contrast is also much less pronounced than for the optimum case, which results in much higher values for optimum contrast in the degraded image for larger breast thicknesses. A possible explanation for this seeming discrepancy is that for images in which the system MTF is included, a larger number of pixels should be considered inside microcalcifications since the outer boundaries of the microcalcifications are spread out due to the smearing effect of the MTF.

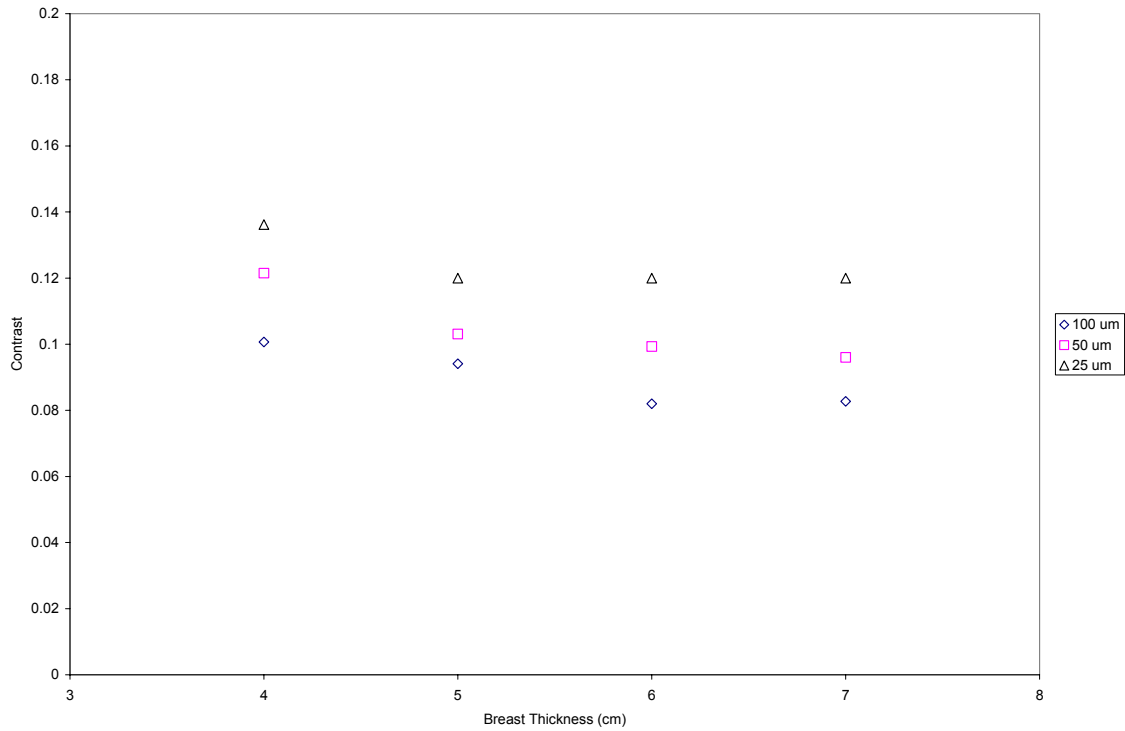


**Figure 4.12 Contrast versus breast thickness for three different detectors. The images used to produce the data in this figure did include the system MTF.**

The main point of interest, however, is that the decrease in contrast for increased breast thickness is minimal no matter which detector type is used.

## Chapter 5

### Summary and Conclusions

The objective of this work was to study three topics commonly discussed in mammography – image resolution, image contrast, and breast compression – and how they are affected by changing a few mammography system parameters: specifically detector pixel size and the degree to which the breast is compressed. It was also mentioned that the hope for newer mammography modalities is that utilizing detectors with significantly smaller pixel sizes would lead to significant improvements in image quality. The results from chapter 4, however, do not show this to be decisively true for all of the parameters studied.

Beginning with section 4.1, we see that image resolution is not significantly impacted by decreasing detector pixel size, as was expected. This is true even in the most ideal case, in which images do not include effects of system MTFs or of quantum mottle. We see that current 100- $\mu\text{m}$  detectors are already fairly good at resolving the microcalcifications in the phantom with about a 90% detection rate for all breast thicknesses for the ideal case. For the non-ideal cases, in which the MTF is included in production of the image, we see that the resolution for all detectors is greatly reduced, but more importantly, the difference between detector types is decreased to only about an 8% difference at best when comparing the 100- and 25- $\mu\text{m}$  detectors. Including quantum mottle would almost certainly decrease this difference even further. This suggests that perhaps developing smaller pixel detectors is not the solution for resolving microcalcification cluster patterns, since it appears that even decreasing the pixel area by a factor of 16 does not produce a significantly better detection rate. Also, one must recall that the MTF for the 50  $\mu\text{m}$  detector was applied to the 100 and

25  $\mu\text{m}$  pixel detectors. If the proper MTFs were available and had been applied in this work, one might expect the 100  $\mu\text{m}$  detector image to decrease in quality, while the image quality for the 25  $\mu\text{m}$  detector might improve. However, this is not certain since addition of quantum mottle may cancel out any of the benefits provided by using the correct MTF for either system.

Continuing on in section 4.1, we do see some positive results when discussing the relationship between pixel size and breast compression. In both the ideal and non-ideal cases, the degrees of breast compression included in this study do not significantly alter the percentage of microcalcifications detected for any given detector size. Again, this is true for all detector sizes, so it could again be said that incorporating small pixel detectors may not be cost effective since current modalities seem to produce similar results to these new systems. But this does bode well for suggesting that breast compression may be reduced when specifically dealing with calcification clusters. However, since this work does not include patient affects, such as chest movement due to breathing, clinical studies would certainly be necessary to verify such a conclusion.

In section 4.2, the focus switched to image contrast, and again, varying pixel size didn't seem to produce a very significant effect on optimum contrast for each image. Smaller-pixel detectors did produce better image contrast, but only slightly better than the 100- $\mu\text{m}$  detector. Again as in the case of resolution, if quantum mottle were added to the images, it is almost certain that this increase would be even less significant.

When considering the affect of varying breast compression on contrast, the result is similar to varying pixel size. As one would expect, a breast that is under greater compression results in an image that has a better contrast. However, again, it is clear from the figures

provided that even over a 3-cm increase in breast thickness, the optimum contrast decreases only by a very insignificant degree – only about 20% or less. So again it appears that a 3-cm increase in breast thickness may result in an acceptable loss of image quality in exchange for an increase in patient comfort.

In conclusion, this study seems to point to two basic points. First, even though decreasing detector pixel dimensions leads to better resolution and contrast as expected, the increase in quality is so small as to be insignificant, especially since even the non-ideal case used in this study was still in some respects ideal since additional noise and mammary artifacts would be present in a true mammogram. If these additions were included in the images, the image quality would certainly be degraded even further.

The second point is that decreasing the degree to which the breast is compressed during a mammogram at least several centimeters can be accomplished without too great a loss in image quality. Again, this result is only based on system parameters, though, and does not include effects on the image that are a direct result of the patient's actions during the mammogram process. This does suggest, though, that it may be prudent to conduct some clinical studies on the effect of decreased breast compression on image quality. If such studies could be conducted with positive confirmation of the results in this work, increasing patient comfort during the mammogram might be greatly improved, which could be deemed the most important factor of all. If patients feel comfortable during their mammograms, then perhaps there will be a much greater acceptance of the mammography screening process among women in general. And of course, getting the patient to the screening is the most important step.

## Bibliography

1. Boone J M, Fewell T R, and Jennings R J, (1997) “Molybdenum, Rhodium, and Tungsten Anode Spectral Models Using Interpolating Polynomials with Applications to Mammography”. *Medical Physics*, **24(12)**, 1863 – 1874.
2. Chan H-P, Lo S-C B, Niklason L T, Ikeda D M, and Lam K W, (1996) “Image Compression in Digital Mammography: Effects on Computerized Detection of Subtle Microcalcifications”. *Medical Physics*, **23(8)**, 1325 – 1336.
3. Chan H-P, Vyborny C J, MacMahon H, Metz C E, Doi K, and Sickles E A, (1987) “Digital Mammography ROC Studies of the Effects of Pixel Size and Unsharp-Mask Filtering on the Detection of Subtle Microcalcifications”. *Investigative Radiology*, **22**, 581 – 589.
4. Cowen A R, Launder J H, Jadav M, Brett D S, (1997) “Visibility of microcalcifications in Computed and Screen-Film Mammography”. *Physics in Medicine and Biology*, **42**, 1533 – 1548.
5. Hermann G, Janus C, Schwarz I S, Papatestas A, Hermann D G, Rabinowitz J G, (1988) “Occult Mammography Lesions in 114 Patients: Relationship to Age and the Presence of Microcalcifications”. *Radiology*, **169**, 321 - 324.
6. ICRU (1992) *ICRU 46: Photon, Electron, Proton and Neutron Interaction Data for Body Tissues* Report 46.
7. Lado M J, Tahoces P G, Souto M, Mendez A J, Vidal J J, (1997) “Real and Simulated Clustered Microcalcifications in Digital Mammograms. ROC Study of Observer Performance”. *Medical Physics*, **24(9)**, 1385 – 1394.

8. Morin R L (Ed.) (1988) *Monte Carlo Simulation in the Radiological Sciences*. Boca Raton, FL: CRC Press. Chan H-P, and Doi K, “Monte Carlo Simulation in Diagnostic Radiology”. (Chapter 5) 103 – 192.
9. Nagel R H, Nishikawa R M, Papaioannou J, and Doi K, (1998) “Analysis of Methods for Reducing False Positives in the Automated Detection of Clustered Microcalcifications in Mammograms”. *Medical Physics*, **25(8)**, 1502 – 1506.
10. Peplow D E, (1999) *Manual for the MCMIS Code System*. Located in the North Carolina State University E-Locker  
[eos.ncsu.edu/service/ne/project/ne\\_med/MCMIS/mcmanual.pdf](http://eos.ncsu.edu/service/ne/project/ne_med/MCMIS/mcmanual.pdf)
11. Peplow D E, (1999) “Monte Carlo Mammography Image Simulation with Measured Coherent Scattering Form Factors and Differential Sampling”. Doctoral Dissertation. North Carolina State University.
12. Peplow D E, and Verghese K, (1998) “Measured Molecular Coherent Scattering Form Factors of Animal Tissues, Plastics and Human Breast Tissue”. *Physics in Medicine and Biology*, **43**, 2431 – 2452.
13. Peplow D E, and Verghese K, (1999) “Digital Mammography Image Simulation Using Monte Carlo”. *Medical Physics*, **27(3)**, 569 – 579.
14. Qian W, Clarke L P, Li H D, Clark R, and Silbiger M L, (1994) “Digital Mammography: M-Channel Quadrature Mirror Filters (QMFs) for Microcalcification Extraction”. *Computerized Medical Imaging and Graphics*, **18(5)**, 301 – 314.
15. Veldkamp W J H, and Karssemeijer (1998) “Accurate Segmentation and Contrast Measurement of Microcalcifications in Mammograms: A Phantom Study”. *Medical Physics*, **25(7)**, 1102 – 1110.

16. Yoshida H, Doi K, Nishikawa R M, Giger M L, and Schmidt R A, (1996) “An Improved Computer-Assisted Diagnostic Scheme Using Wavelet Transform for Detecting Clustered Microcalcifications in Digital Mammograms”. *Academic Radiology*, **3(8)**, 621 – 627.

## Appendices

# Appendix I

## User Defined Input for MCMIS

This appendix includes an example of the 4 user provided input files necessary to run a simulation with MCMIS for a monoenergetic source. As mentioned in Chapter 3, to produce an entire image, a series of monoenergetic runs must be performed and the output from each combined into a single polyenergetic image. However, only the input files for the case in which a 4-cm breast over a detector with 100- $\mu$ m pixel size is exposed to 5 keV photons will be used in the interest of space. All other input files are located in the NCSU NE medical e-locker at the path

`/afs/eos.ncsu.edu/service/ne/project/ne_med/microcalcs/clusters/`.

Separate sub-directories from this path are used to store information for a single run based on pixel size, breast thickness, and photon energy.

The majority of the information in this appendix is taken from the *Manual for the MCMIS Code System* (Peplow 1999), which is also located in the NCSU NE medical e-locker in PDF form at the path

`/afs/eos.ncsu.edu/service/ne/project/ne_med/MCMIS/mcmanual.pdf`.

There, a user can find a very detailed description of the MCMIS code including batch processing, code libraries, code output, and differential sampling options.

## I.1 Materials

The first user defined input file is the file in which all materials included in a simulation are defined. This file is labeled “mater.inp”. The materials available for MCMIS are included in two library files, “atomic.lib” and “molec.lib”. The first of these libraries contains materials for which the atomic form factors are used during the simulation. The second library contains materials for which molecular form factors are used.

Entries in this file consist of two integers per material. The first integer should be either a 1 or 2. This value denotes the library in which the material can be found; a value of 1 indicates that the atomic form factor library contains the appropriate material data, while a value of 2 indicates that the molecular form factor library should be used. The second entry denotes the material that will be used from the given library.

The following data comes from the materials input file used in this work. Since all of the parameters varied in this work were material independent, this file did not need to change for any case during the simulation runs. A brief description of each material type is included here to clarify what each entry means, and was not present in the actual input file.

```
2 15 ! Molecular Form Factor Library, Breast 50/50 water/lipid
1 30 ! Atomic Form Factor Library, Bone mineral-hydroxyapatite (calcifications)
1 13 ! Atomic Form Factor Library, Air
1 18 ! Atomic Form Factor Library, Polyethylene terephthalate (compression paddle)
1 29 ! Atomic Form Factor Library, Multi-Ply carbon fiber/resin (breast support)
```

## I.2 Geometry

The next user defined input file is the file used to set up the geometry of the simulation. This file is labeled “geom.inp”. The user can choose from 7 different shapes to include in this file, which can be nested to any level desired by the user. The entries for each object in this file include 2 integers, and 9 floating-point numbers. They are listed in the following fashion:

$$m \ n \ x_0 \ y_0 \ z_0 \ p_1 \ p_2 \ p_3 \ p_4 \ p_5 \ p_6$$

where  $m$  denotes the shape of the object (Table I.1),  $n$  is the number of the material from mater.inp,  $(x_0 \ y_0 \ z_0)$  is the center of the object in Cartesian coordinates, and  $p_1$  through  $p_6$  are the parameters that describe the size and orientation of the object.

m	Region	Parameters
1	sphere	Radius
2	z-axis cylinder	radius, height (in z-direction)
3	rectangular box	width (x-dimension), depth (y), height (z)
4	cylinder	radius, height, $\langle v_x, v_y, v_z \rangle$ (direction vector of axis)
5	boiler plate	inner radius, outer radius, length (y dimension), arc angle in radians (in x-z plane)
6	sphere segment	base radius, height (z-dimension)
7	elliptical half-cylinder	minor radius, major radius, height (z-dimension)

**Table I.1 The seven basic shapes for the geom.inp file and their associated parameters. This table is taken from *Manual for the MCMIS Code System* (Peplow 99).**

The following data is the geometry-input file used for all cases in which a 4-cm thick breast was used. The first 5 rows describe the overall geometry of the mammography system and breast phantom. The first row defines the air gap that surrounds the remainder of the

geometry. The second and third rows designate the geometries for the compression paddle and the breast support, respectively. The fourth and fifth rows designate the geometry of the breast region. Recall from Chapter 2 that two regions are needed for the breast in order to simulate a layer of skin surrounding the breast material.

The remaining 128 rows of values make up the microcalcification phantom. Each group of 8 rows makes up a column of microcalcifications. Therefore, two groups make up a column of cluster pairs. For example, the 1<sup>st</sup> group of calcification values below makes up the left-most column of 400- $\mu$ m calcifications, with the second group of values defining the corresponding 50- $\mu$ m calcifications. In order to add some clarification to this explanation, additional comments have been added before each group of numbers. Again, additional comments were not included in the actual input file.

**! Mammography system and breast phantom regions**

```
5 3 0.00000000 9.00000000 61.59913635 1.00000000 62.20000000 20.00000000 0.45000000 0.00000000 0.00000000
5 4 0.00000000 9.00000000 61.60113635 57.89900000 58.04900000 18.00000000 0.42000000 0.00000000 0.00000000
5 5 0.00000000 9.00000000 61.60013635 62.05000000 62.20000000 18.00000000 0.42000000 0.00000000 0.00000000
5 1 0.00000000 7.50000000 61.60213635 58.05000000 62.05000000 15.00000000 0.19339243 0.00000000 0.00000000
5 1 0.00000000 7.50000000 61.60313635 58.15000000 61.95000000 14.80000000 0.19047619 0.00000000 0.00000000
```

**! Microcalcification phantom, cluster column 1, 400  $\mu$ m calcifications**

```
1 2 -0.74750000 6.99250000 1.55213635 0.02000000 0.00000000 0.00000000 0.00000000 0.00000000 0.00000000
1 2 -0.74750000 7.13750000 1.55213635 0.02000000 0.00000000 0.00000000 0.00000000 0.00000000 0.00000000
1 2 -0.74750000 7.28250000 1.55213635 0.02000000 0.00000000 0.00000000 0.00000000 0.00000000 0.00000000
1 2 -0.74750000 7.42750000 1.55213635 0.02000000 0.00000000 0.00000000 0.00000000 0.00000000 0.00000000
1 2 -0.74750000 7.57250000 1.55213635 0.02000000 0.00000000 0.00000000 0.00000000 0.00000000 0.00000000
1 2 -0.74750000 7.71750000 1.55213635 0.02000000 0.00000000 0.00000000 0.00000000 0.00000000 0.00000000
1 2 -0.74750000 7.86250000 1.55213635 0.02000000 0.00000000 0.00000000 0.00000000 0.00000000 0.00000000
1 2 -0.74750000 8.00750000 1.55213635 0.02000000 0.00000000 0.00000000 0.00000000 0.00000000 0.00000000
```

**! Microcalcification phantom, cluster column 1, 50  $\mu$ m calcifications**

```
1 2 -0.70500000 6.99250000 1.55213635 0.00250000 0.00000000 0.00000000 0.00000000 0.00000000 0.00000000
1 2 -0.70750000 7.13750000 1.55213635 0.00250000 0.00000000 0.00000000 0.00000000 0.00000000 0.00000000
1 2 -0.71000000 7.28250000 1.55213635 0.00250000 0.00000000 0.00000000 0.00000000 0.00000000 0.00000000
1 2 -0.71250000 7.42750000 1.55213635 0.00250000 0.00000000 0.00000000 0.00000000 0.00000000 0.00000000
1 2 -0.71500000 7.57250000 1.55213635 0.00250000 0.00000000 0.00000000 0.00000000 0.00000000 0.00000000
1 2 -0.71750000 7.71750000 1.55213635 0.00250000 0.00000000 0.00000000 0.00000000 0.00000000 0.00000000
1 2 -0.72000000 7.86250000 1.55213635 0.00250000 0.00000000 0.00000000 0.00000000 0.00000000 0.00000000
1 2 -0.72250000 8.00750000 1.55213635 0.00250000 0.00000000 0.00000000 0.00000000 0.00000000 0.00000000
```





! Microcalcification phantom, cluster column 8, 400  $\mu\text{m}$  calcifications (left pair member)

```
1 2 0.68750000 6.99250000 1.55213635 0.02000000 0.00000000 0.00000000 0.00000000 0.00000000 0.00000000
1 2 0.68750000 7.13750000 1.55213635 0.02000000 0.00000000 0.00000000 0.00000000 0.00000000 0.00000000
1 2 0.68750000 7.28250000 1.55213635 0.02000000 0.00000000 0.00000000 0.00000000 0.00000000 0.00000000
1 2 0.68750000 7.42750000 1.55213635 0.02000000 0.00000000 0.00000000 0.00000000 0.00000000 0.00000000
1 2 0.68750000 7.57250000 1.55213635 0.02000000 0.00000000 0.00000000 0.00000000 0.00000000 0.00000000
1 2 0.68750000 7.71750000 1.55213635 0.02000000 0.00000000 0.00000000 0.00000000 0.00000000 0.00000000
1 2 0.68750000 7.86250000 1.55213635 0.02000000 0.00000000 0.00000000 0.00000000 0.00000000 0.00000000
1 2 0.68750000 8.00750000 1.55213635 0.02000000 0.00000000 0.00000000 0.00000000 0.00000000 0.00000000
```

! Microcalcification phantom, cluster column 8, 400  $\mu\text{m}$  calcifications (right pair member)

```
1 2 0.74750000 6.99250000 1.55213635 0.02000000 0.00000000 0.00000000 0.00000000 0.00000000 0.00000000
1 2 0.74500000 7.13750000 1.55213635 0.02000000 0.00000000 0.00000000 0.00000000 0.00000000 0.00000000
1 2 0.74250000 7.28250000 1.55213635 0.02000000 0.00000000 0.00000000 0.00000000 0.00000000 0.00000000
1 2 0.74000000 7.42750000 1.55213635 0.02000000 0.00000000 0.00000000 0.00000000 0.00000000 0.00000000
1 2 0.73750000 7.57250000 1.55213635 0.02000000 0.00000000 0.00000000 0.00000000 0.00000000 0.00000000
1 2 0.73500000 7.71750000 1.55213635 0.02000000 0.00000000 0.00000000 0.00000000 0.00000000 0.00000000
1 2 0.73250000 7.86250000 1.55213635 0.02000000 0.00000000 0.00000000 0.00000000 0.00000000 0.00000000
1 2 0.73000000 8.00750000 1.55213635 0.02000000 0.00000000 0.00000000 0.00000000 0.00000000 0.00000000
```

### I.3 Source and Detector

Another input file required from the user is the source/detector file. This file includes the parameters that describe the source/detector system that will be used for a given case and is called sode.inp. Both the source and detector information should be given in the form:

$$m \ n \ x_0 \ y_0 \ z_0 \ p_1 \ p_2 \ p_3 \ p_4 \ \dots \ p_n$$

where  $m$  is an integer specifying which source (detector) type is used,  $n$  is an integer that specifies the number of parameters that are used to describe that source (detector) type, and  $p_1$  to  $p_n$  are the parameters that describe the position, size, and other necessary parameters for the source (detector) type chosen. The final entry to the sode.inp file is the pertinent information for the phosphor material of the detector. The phosphor information should be given in the form:

$$m \ p_1 \ p_2$$

where  $m$  is an integer specifying the phosphor type,  $p_1$  is the density thickness of the material, and  $p_2$  is the thickness of the material.

Table I.2 and Table I.3 list the source and detector types available for MCMIS simulations and the parameters required for each. Also, Table I.4 lists the various detector phosphor types available.

m	n	Description and Parameters
1	15	parallel beam, from a rastered area 1 energy in keV; 2-4 center of source rectangle; 5,6 size of source area (cm); 7,8 number of x and y pixels for flash image; 9,10 number of pixels for the coarse mesh images; 11 polarized? yes (1) or not (0); 12-14 direction of polarization (must be included, whether or not beam is polarized); 15 beam size in scan direction (cm). Note: photon emission direction is always (0,0,-1).
2	13	divergent point source over a curved target 1 energy in keV; 2-4 location of point source; 5 source to target distance (SID) in cm; 6 y-dimension of target grid in cm; 7,8 limits in angle (radians) or target grid; 9,10 number of x and y pixels for flash image; 11,12 number of x and y pixels for coarse mesh images; 13 beam size in scan direction (in radians).
3	11	pencil beam 1 energy in keV; 2-4 center of source rectangle; 5-7 direction cosines of beam; 8 polarized? yes (1) or not (0); 9-11 direction of polarization (must be included, whether or not beam is polarized).
4	14	divergent point source over a planar target 1 energy in keV; 2-4 location of point source; 5-7 center of target rectangle; 8,9 size of source area (cm); 10,11 number of x and y pixels for flash image; 12,13 number of x and y pixels for course mesh images; 14 beam size in scan direction (in cm).

**Table I.2 Available source types for the sode.inp input file and their associated parameters. This table is taken from *Manual for the MCMIS Code System* (Peplow 99).**

m	n	Description and Parameters
1	13	rectangular planar area detector grid, perpendicular to z-axis, scanned in y direction, with active area y width 1-3 center of detector rectangle; 4-5 size of detector area; 6-7 pixels-x, pixels-y unscattered image; 8-9 pixels-x, pixels-y scattered image; 10 active area width in scan direction (in cm); 11 phosphor material type; 12 phosphor material density thickness; 13 phosphor thickness
2	15	cylindrical wall detector grid, axis parallel to y-axis, covering only a portion, from $\theta_l$ to $\theta_u$ (as observed from the detector center point), scanned in x (curved) direction, with active area x width 1-3 reference point (x of cyl axis, low y, z of cyl axis); 4-5 SID, size in y direction; 6-7 pixels-x, pixels-y unscattered image; 8-9 pixels-x, pixels-y scattered image; 10-11 $\theta_l$ , $\theta_u$ limits in angle (in radians); 12 size of active area, in direction of scan (radians); 13 phosphor material type; 14 phosphor material density thickness; 15 phosphor thickness
3	5	circular planar area detector grid, concentric ring pixels in x-y plane, not used with point detectors, perfectly absorbing 1-3 center of detector; 4 maximum radius; 5 how many radial rings

**Table I.3 Available detector types for the sode.inp input file and their associated parameters. This table is taken from *Manual for the MCMIS Code System* (Peplow 99).**

m	Description and Nominal Parameters
1	perfect detector, full energy is absorbed in pixel
2	Geiger counter type, a unit value is absorbed, independent of the energy of the Photon
3	BaFBr <sub>0.85</sub> I <sub>0.15</sub> , photostimulable phosphor, density thickness of Fuji ST and HR plates are 0.033 g/cm <sup>2</sup> and 0.048 g/cm <sup>2</sup> , both are about 0.015 cm thick.
4	CsI, CCD material, new Fischer Senoscan detector is 0.06765 g/cm <sup>2</sup> and 0.015 cm Thick

**Table I.4 Phosphor types available for the sode.inp file with appropriate density thickness and thickness values (where applicable). This table is taken from *Manual for the MCMIS Code System* (Peplow 99).**

The following data is the source/detector set-up input file used for a source emitting 5 keV photons, and a detector that has 100- $\mu\text{m}$  pixels. Again, the source and detector chosen for this and all other cases were chosen in order to simulate as closely as possible the Fischer Senoscan. Also, all comments included here were absent in sode.inp.

```

2 13 ! source type: divergent point source over a curved target
5.0 0.0 0.0 61.59232259 63.80000000 18.0 ! source energy, location, SID, and y-dim
-0.1410658307 0.1410658307 ! limits of target grid (radians)
1800 1800 ! flash image pixels
36 36 ! coarse mesh image pixels
0.0203761755 ! beam size in scan direction
2 15 ! detector type: cylindrical wall detector grid (curved detector)
0.0 0.0 61.59232259 63.80000000 15.0 ! SID, y-dim
400 1500 ! flash image pixels
8 30 ! coarse mesh image pixels
-0.0313479624 0.0313479624 !  $\theta_l$ ,  $\theta_u$ 
0.0156739812 ! size of active area in scan direction
4 ! phosphor type: CsI (CCD material)
0.06765 ! phosphor density thickness
0.0150 ! phosphor thickness

```

## I.4 Monte Carlo Parameters

The final user defined input file required contains the necessary Monte Carlo information and is called mc.inp. This file contains 3 integers, 1 floating-point number, and five ForTran logical statements. The first two integers dictate how many histories will be used for a simulation. The first integer sets the number of outer iterations. After each outer iteration, output is dumped to file so that simulation progress can be monitored while the simulation is still running. This allows the user to halt a simulation prior to completion if a

problem is noticed. This is especially useful since an entire run can take several hours. The second integer sets the number of histories used for each outer iteration. This number should be set as a multiple of the total number of coarse mesh pixels so that each pixel in the source grid gets the same number of histories. The third integer is the random number seed. The only requirements for this parameter are that it should be large, odd, and different for each simulation run. The floating-point number is the Russian roulette minimum weight. The five logical statements determine which components of MCMIS will be used in the MC simulation. For all five of these options a value of “.true.” means that the option is enabled, and a value of “.false.” means that the option will not be used. The following table describes what each of the five logical statements controls:

Logical Statement	Option
1	relativistic form factors
2	x-ray fluorescence after photoelectric effect
3	point detector scheme
4	implicit capture
5	Last flight estimator

**Table I.5 Description of the 5 logical statements necessary for the mc.inp input file.**

The following data is the set of Monte Carlo parameters used for the simulation case of interest in this appendix. A brief description is given for each row.

8 12960 ! 8 outer loops, 12960 inner loops (total of 103680 loops)  
40541 ! random number seed  
0.0001 ! Russian roulette minimum weight  
.true. ! Relativistic form factors are used.  
.false. ! No x-ray fluorescence after photoelectric effect.  
.true. ! Point detector scheme is used.  
.true. ! Implicit capture is used.  
.true. ! Last flight estimator is used.

## Appendix II

### Image Production and Analysis Codes

As mentioned in chapter 3, MCMIS doesn't create the final simulated images that we require for this study. Instead, it produces several output files that must be combined using the process that was also outlined in that chapter. After the images are processed, then analysis can be completed on them; the analysis procedure was also discussed in chapter 3. The purpose of this appendix is to provide the interested reader with the Matlab™ routines used both for image production and analysis. Also, a section is included to show all images that were not included in the main body of this text.

#### II.1 Image Production Code

This section contains the Matlab™ code used to produce the images from the output files of MCMIS. Dr. Peplow created this Matlab™ routine for use in his doctoral thesis. Minor additions were made for organizational reasons only. However, none of the code used for incorporating MCMIS output into image files was altered. Comments are included throughout the code in order to explain the image production process. A brief outline of the code algorithm is given here, as well.

##### II.1.1 Algorithm

1. Set up necessary information for code execution. This includes setting up proper directories, setting variable lengths, and reading in pertinent user defined information (i.e. breast thickness, pixel size, and kVp setting).
2. Read in proper spectrum using the Boone routine. Integrate spectrum around a given Monte Carlo energy to calculate weights for a given energy.

3. Read in MCMIS output for each individual energy in spectrum and weight it accordingly with weights determined in step (2). After they are properly weighted, add images up for total image.
4. Interpolate poly-energetic coarse mesh image to fit poly-energetic flash image. Add these together to make complete image that includes both scattered and unscattered contributions.
5. Add poison distributed noise to image. (This was done for all images in this work, but the images were not included in the analysis.)
6. Smear image with Fischer system MTF.
7. Output image to screen, and save all necessary files to disk.

## II.1.2 Code

```

function [con] = polyg(ikVp,ibt,ps)
%=====
% Author   : Douglas E. Peplow
% Date     : July 9, 1998
% Ammendments: Gary B. Zeigler, II
% Date     : February 20, 2001
% Purpose  : Combine monoenergetic images into a poly energetic
%           image. This is for the runs in /local/gbzeigle* and
%           /local2/gbzeigle* of dunes.ne.ncsu.edu
%
% Series   : Code12
%
% Input    : ikVp  which fkVp setting 3-5 for [30 35 40]
%           ibt   breast thickness: 1-4cm, 2-5cm, 3-6cm, 4-7cm
%           ps    pixel size: 1-100micron, 2-50micron,
%                 3-25micron
%
%=====

path(path,'/afs/eos/service/ne/project/ne_med/MCMIS/Matlab')

if ibt==1
    path='/local/gbzeigle.dir';    % 4cm breast thickness files
elseif ibt==2
    path='/local/gbzeigle3.dir';  % 5cm breast thickness files
elseif ibt==3
    path='/local2/gbzeigle4.dir'; % 6cm breast thickness files
elseif ibt==4
    path='/local2/gbzeigle.dir';  % 7cm breast thickness files

```

```

else
  disp([' Stop!  ibt must be 1, 2, 3, or 4']);
end;

dirs=['e05e06e07e08e09e10'...
      'e11e12e13e14e15e16e17e18e19e20'...
      'e21e22e23e24e25e26e27e28e29e30'...
      'e31e32e33e34e35e36e37e38e39e40'];
mcener=5:40;
files=['flash ', 'unscat ', 'scat ', 'unscaterr', 'scaterr '];
flen=[5 6 4 9 7];
dirmax=[26 31 36];

if ps==1
  fdetx=400; fdety=1500; ndetx=8; ndety=30;
elseif ps==2
  fdetx=800; fdety=800; ndetx=16; ndety=16;
elseif ps==3
  fdetx=1000; fdety=1000; ndetx=20; ndety=20;
else
  display([' Stop!  ps must be 1, 2, or 3']);
end;

if ikVp<3 | ikVp>5
  disp([' Stop.  ikVp must be 3, 4 or 5']);
end;

fac= 0.0156739812/0.0203761755; % sode.inp, dgap/play

%-----
% Call the Boone routine to get the energy spectrum of the tube/filter
% Integrate a portion of the Boone spectra around an MC energy
%
% Run this three times: W anode, 30 kVp, Al filter, 0.0500 cm
%           W anode, 35 kVp, Al filter, 0.0500 cm
%           W anode, 40 kVp, Al filter, 0.0500 cm
%
%-----

[spener,spectrum]=boonesp(3,ikVp,1,0.0500,0.05,0);

spectrum=spectrum/max(spectrum);
weight=zeros(size(mcener));
k=1;
for i=1:dirmax(ikVp-2)

```

```

ener=mcener(i);
for j=1:90
    if spener(j)==ener
        k=j;
        end;
    end;
weight(i)=0.5*(spectrum(k-1)+spectrum(k))*(spener(k)-spener(k-1)) + ...
    0.5*(spectrum(k)+spectrum(k+1))*(spener(k+1)-spener(k));
end;
weight=weight/sum(weight);

%-----
% Now that the weights are done, add up the individual images
%-----

comstr=['cd ' path];
eval(comstr);

polyfl = zeros(fdety,fdetx);
polyun = zeros(ndety,ndetx);
polysc = zeros(ndety,ndetx);
polyune = zeros(ndety,ndetx);
polysce = zeros(ndety,ndetx);

disp('Looping through Monte Carlo files ');
for i=1:dirmax(ikVp-2)
    disp([' ' path '/' dirs(3*i-2:3*i) ]);
    j=1;
    filename=[ path '/' dirs(3*i-2:3*i) '/' ...
        files(9*(j-1)+1:9*(j-1)+flen(j) )];
    comstr=[' mc' num2str(j,1) '=binread('' filename ...
        '', fdety,fdetx );'];
    eval( comstr );
    for j=2:5
        filename=[ path '/' dirs(3*i-2:3*i) '/' ...
            files(9*(j-1)+1:9*(j-1)+flen(j) )];
        comstr=[' mc' num2str(j,1) '=binread('' filename ...
            '', ndety,ndetx );'];
        eval( comstr );
    end;

    polyfl = polyfl + weight(i)*mc1;
    polyun = polyun + weight(i)*mc2;
    polysc = polysc + weight(i)*mc3;
    polyune = polyune + weight(i)*mc4.*mc4;

```

```

    polysce = polysce + weight(i)*mc5.*mc5;
end;
polyune=sqrt(polyune);
polysce=sqrt(polysce);
disp(' ');

%-----
% Account for slitsize and source beam size
%-----

polyfl = polyfl*fac ;

%-----
% Put the poly images back into the main directory
% save as matlab files, ForTran will probably not need to read these.
%-----

comstr=['cd ' path];
eval(comstr);
disp('Saving Poly images ');
eval(['cd ' path]);
binwrite('polyfl', polyfl, fdety,fdetx);
binwrite('polyun', polyun, ndety,ndetx);
binwrite('polysc', polysc, ndety,ndetx);
binwrite('polyune',polyune,ndety,ndetx);
binwrite('polysce',polysce,ndety,ndetx);

%-----
%
% Interpolate the scatter map and add 'em up (remember to equalize!)
% Since center points of fine meash are out of bounds of course
% mesh, move (fudge) the outer edges of the course mesh
%-----

disp('Creating final and smeared image ');
term=ndetx*ndety/fdetx/fdety;

if(ps==1)
xsize=4.0;ysize=15.0;
end;
if(ps==2)
xsize=4.0;ysize=4.0;
end;
if (ps==3)
xsize=2.5;ysize=2.5;

```

```

end;
dxl=xsize/ndetx;dyl=ysize/ndety;
bigx=0.5*dxb:dxb:xsize-0.5*dxb;
bigy=0.5*dyl:dyl:ysize-0.5*dyl;
litx=0.5*dxl:dxl:xsize-0.5*dxl;
lity=0.5*dyl:dyl:ysize-0.5*dyl;
litx(1)=0.0;litx(ndetx)=xsize;
lity(1)=0.0;lity(ndety)=ysize;

wowss=interp2(litx,lity',polysc, bigx,bigy');
wow=wowss*term+polyfl;

%-----
% How much will the Senoscan smear noise?
% assumption - noise is poisson distributed
%-----

if ps==1 % noise addition for 100 micron image
    test=random('norm',0,1,100,100); % 1) create test 100x100 test matrix
    stest=smearf(1,test,0.01,0); % 2) smear test matrix with senoscan mtf
    sigreduc =mean( std(stest(11:90,11:90))); % 3) find mean value of st.dev. in each
    % column of smeared test matrix
    sig=(0.005/sigreduc)*wow; % 4) multiply poisson noise/white noise by
    % combined image to get sig
    noise=random('norm',0,sig); % 5) create noise matrix by choosing random value
    % between zero and value of sig for each pixel in sig
    noisy=wow+noise; clear noise; % 6) add noise matrix to combined image matrix
elseif ps==2 % noise addition for 50 micron image
    test=random('norm',0,1,100,100);
    stest=smearf(1,test,0.005,0);
    sigreduc =mean( std(stest(11:90,11:90)));
    sig=(0.01/sigreduc)*wow;
    noise=random('norm',0,sig);
    noisy=wow+noise; clear noise;
elseif ps==3 % noise addition for 25 micron image
    test=random('norm',0,1,100,100);
    stest=smearf(1,test,0.0025,0);
    sigreduc =mean( std(stest(11:90,11:90)));
    sig=(0.02/sigreduc)*wow;
    noise=random('norm',0,sig);
    noisy=wow+noise; clear noise;
end;

%-----

```

```

% smear it with Fischer MTF
%-----

if ps==1 % apply mtf to 100 micron image
    mo=smearf(1,wow,0.0100,0);
    sm=smearf(1,noisy,0.0100,0);
elseif ps==2 % apply mtf to 50 micron image
    mo=smearf(1,wow,0.0050,0);
    sm=smearf(1,noisy,0.0050,0);
elseif ps==3 % apply mtf to 25 micron image
    mo=smearf(1,wow,0.0025,0);
    sm=smearf(1,noisy,0.0025,0);
end;

%-----
% Show the final product
%-----

% total image including scatter, MTF, and additional noise

figure(1);
imagesc(sm);
axis('xy');
axis('image');
colormap(bone);
axis('off');
axis('equal');

% image that includes only unscattered and scatter photons, and MTF

figure(2);
imagesc(mo);
axis('xy');
axis('image');
colormap(bone);
axis('off');
axis('equal');

% image that includes only scattered and unscattered photons

figure(3);
imagesc(un);
axis('xy');
axis('image');
colormap(bone);

```

```

axis('off');
axis('equal'

%-----
% Save appropriate file
%-----
comstr=['cd ' path];
eval(comstr);
if(ps==1)
    if(ibt==1)
        binwrite('40sm100p4b',sm,fdety,fdetx);
        binwrite('40mo100p4b',mo,fdety,fdetx);
        binwrite('40un100p4b',wow,fdety,fdetx);
        saystr=['Files for 4 cm image have been written to ' path];
        disp(saystr);
    end;
    if(ibt==2)
        binwrite('40sm100p5b',sm,fdety,fdetx);
        binwrite('40mo100p5b',mo,fdety,fdetx);
        binwrite('40un100p5b',wow,fdety,fdetx);
        saystr=['Files for 5 cm image have been written to ' path];
        disp(saystr);
    end;
    if(ibt==3)
        binwrite('40sm100p6b',sm,fdety,fdetx);
        binwrite('40mo100p6b',mo,fdety,fdetx);
        binwrite('40un100p6b',wow,fdety,fdetx);
        saystr=['Files for 6 cm image have been written to ' path];
        disp(saystr);
    end;
    if(ibt==4)
        binwrite('40sm100p7b',sm,fdety,fdetx);
        binwrite('40mo100p7b',mo,fdety,fdetx);
        binwrite('40un100p7b',wow,fdety,fdetx);
        saystr=['Files for 7 cm image have been written to ' path];
        disp(saystr);
    end;
end;
if(ps==2)
    if(ibt==1)
        binwrite('40sm50p4b',sm,fdety,fdetx);
        binwrite('40mo50p4b',mo,fdety,fdetx);
        binwrite('40un50p4b',wow,fdety,fdetx);
        saystr=['Files for 4 cm image have been written to ' path];
        disp(saystr);
    end;
end;

```

```

end;
if(ibt==2)
    binwrite('40sm50p5b',sm,fdety,fdetx);
    binwrite('40mo50p5b',mo,fdety,fdetx);
    binwrite('40un50p5b',wow,fdety,fdetx);
    saystr=['Files for 5 cm image have been written to ' path];
    disp(saystr);
end;
if(ibt==3)
    binwrite('40sm50p6b',sm,fdety,fdetx);
    binwrite('40mo50p6b',mo,fdety,fdetx);
    binwrite('40un50p6b',wow,fdety,fdetx);
    saystr=['Files for 6 cm image have been written to ' path];
    disp(saystr);
end;
if(ibt==4)
    binwrite('40sm50p7b',sm,fdety,fdetx);
    binwrite('40mo50p7b',mo,fdety,fdetx);
    binwrite('40un50p7b',wow,fdety,fdetx);
    saystr=['Files for 7 cm image have been written to ' path];
    disp(saystr);
end;
end;
if(ps==3)
    if(ibt==1)
        binwrite('40sm25p4b',sm,fdety,fdetx);
        binwrite('40mo25p4b',mo,fdety,fdetx);
        binwrite('40un25p4b',wow,fdety,fdetx);
        saystr=['Files for 4 cm image have been written to ' path];
        disp(saystr);
    end;
    if(ibt==2)
        binwrite('40sm25p5b',sm,fdety,fdetx);
        binwrite('40mo25p5b',mo,fdety,fdetx);
        binwrite('40un25p5b',wow,fdety,fdetx);
        saystr=['Files for 5 cm image have been written to ' path];
        disp(saystr);
    end;
    if(ibt==3)
        binwrite('40sm25p6b',sm,fdety,fdetx);
        binwrite('40mo25p6b',mo,fdety,fdetx);
        binwrite('40un25p6b',wow,fdety,fdetx);
        saystr=['Files for 6 cm image have been written to ' path];
        disp(saystr);
    end;
end;

```

```
if(ibt==4)
    binwrite('40sm25p7b',sm,fdety,fdetx);
    binwrite('40mo25p7b',mo,fdety,fdetx);
    binwrite('40un25p7b',wow,fdety,fdetx);
    saystr=['Files for 7 cm image have been written to ' path];
    disp(saystr);
end;
end;
clear sm;
```

## II.2 Additional Images

Many images were created for this work that were not included as figures in the main body of the text. All images were used in analysis, though, and are therefore included here for those interested in comparing visually all images that were produced. The images presented here do not include those that were used in chapter 4. Therefore, the 4 cm images produced using a 100  $\mu\text{m}$  detector, the 4 cm images produced using a 25  $\mu\text{m}$  detector, and the 7 cm images produced using a 25  $\mu\text{m}$  detector do not appear here. For all images included in this section, the unsmear image is on the left hand side of the figure, while the image smeared with the system MTF is on the right.

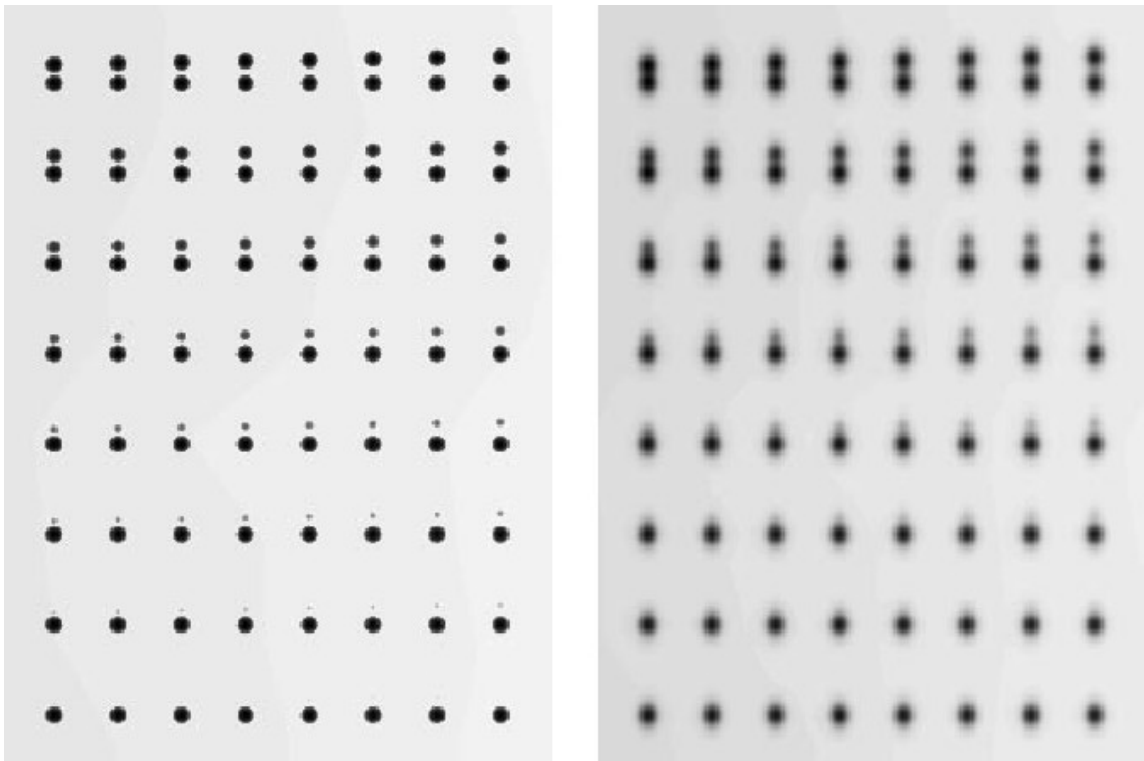


Figure II.1 Images of a 4 cm breast produced using a 50  $\mu\text{m}$  pixel detector.

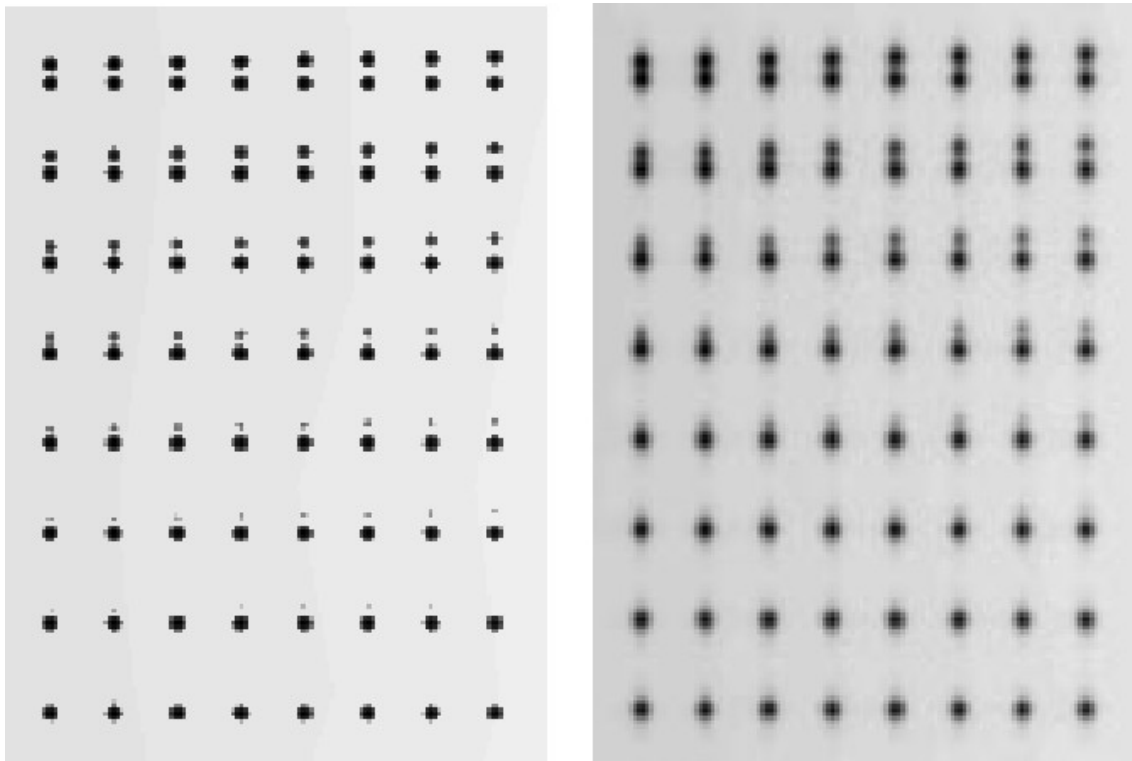


Figure II.2 Images of a 5 cm breast produced using a 100  $\mu\text{m}$  pixel detector.

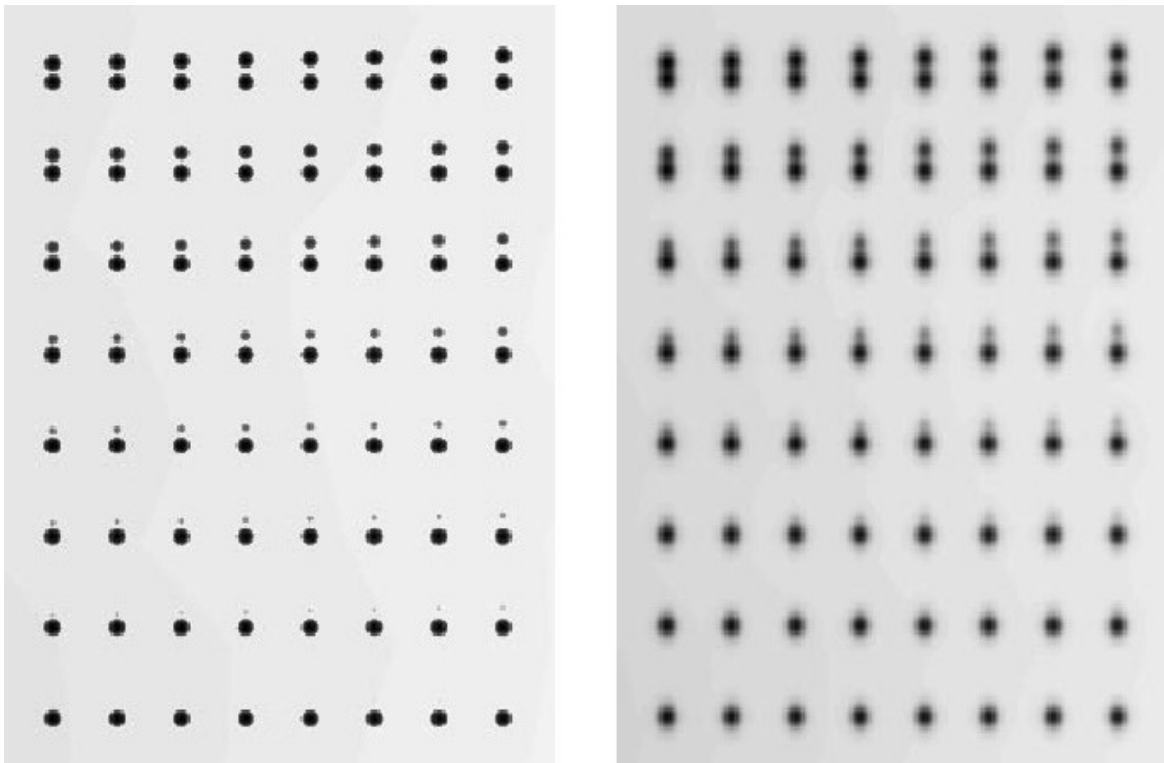


Figure II.3 Images of a 5 cm breast produced using a 50  $\mu\text{m}$  pixel detector.

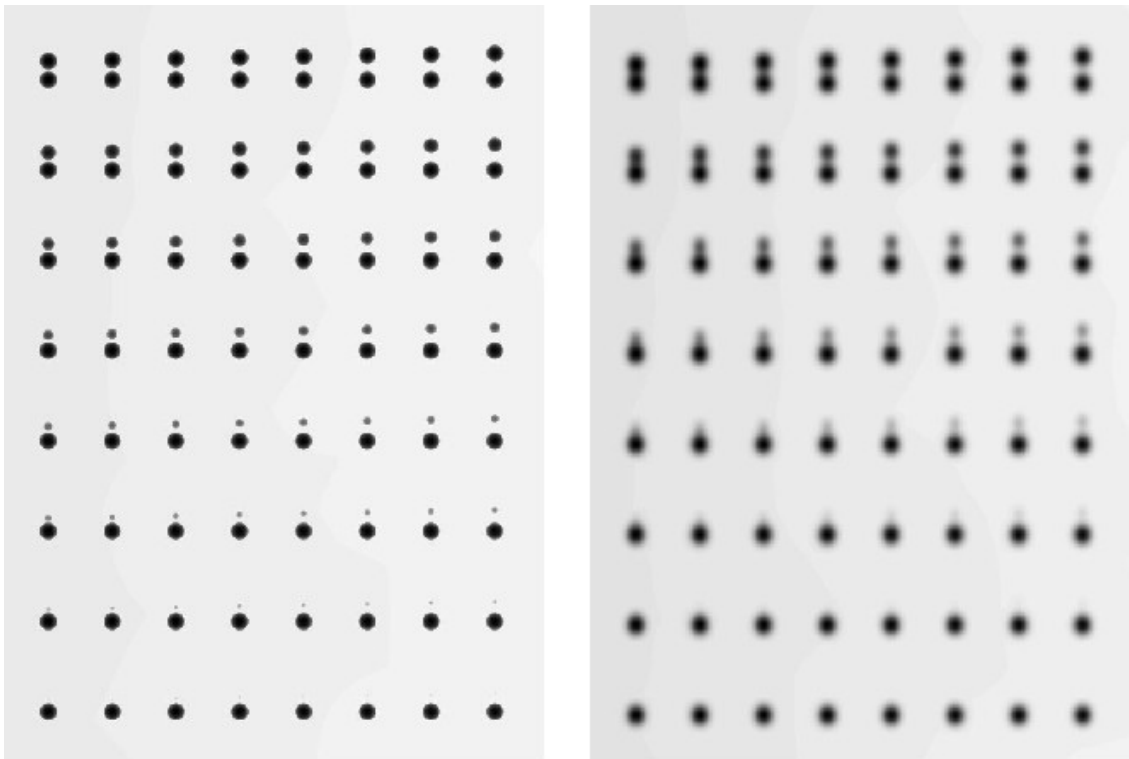


Figure II.4 Images of a 5 cm breast produced using a 25  $\mu\text{m}$  pixel detector.

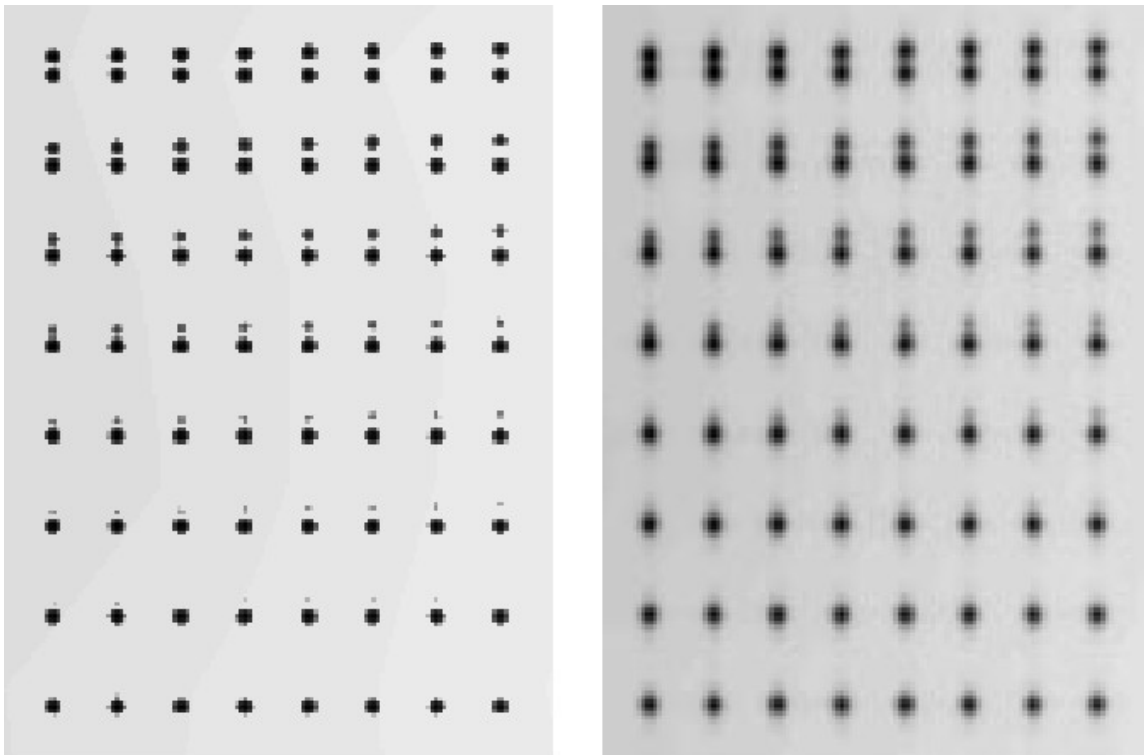


Figure II.5 Images of a 6 cm breast produced using a 100  $\mu\text{m}$  pixel detector.

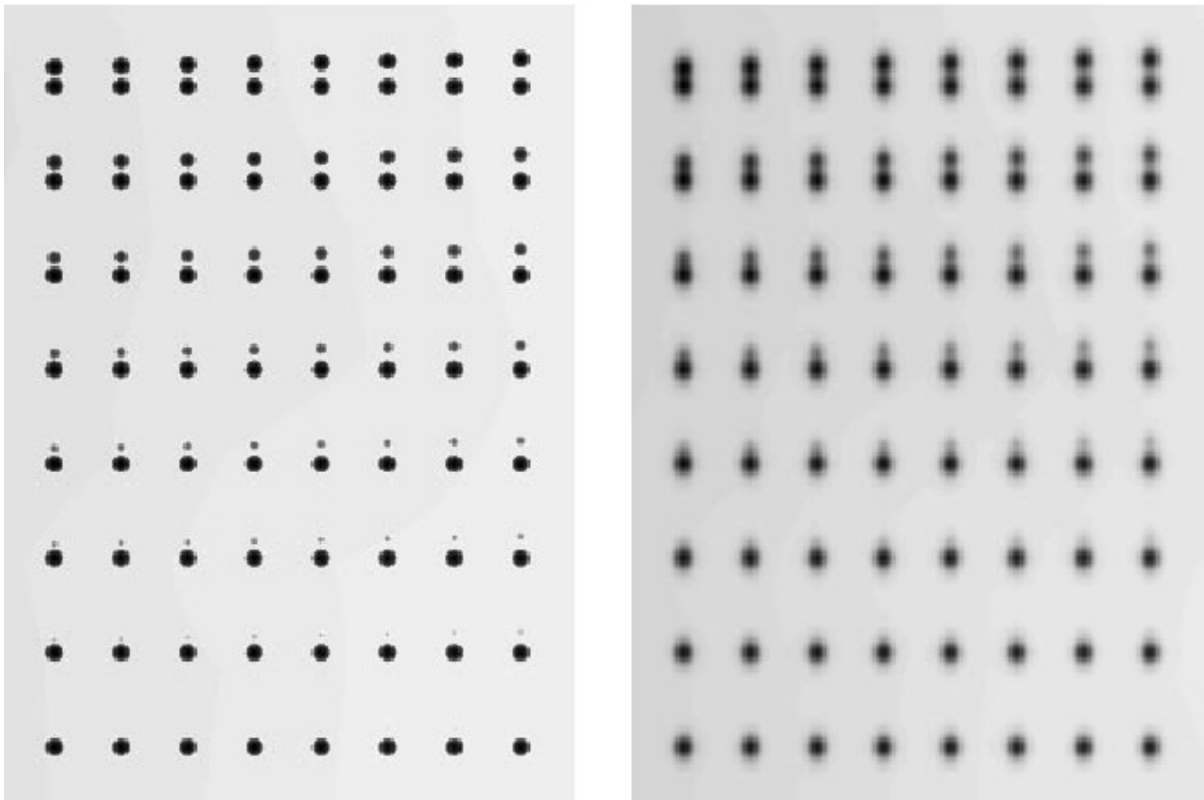


Figure II.6 Images of a 6 cm breast produced using a 50  $\mu\text{m}$  pixel detector.

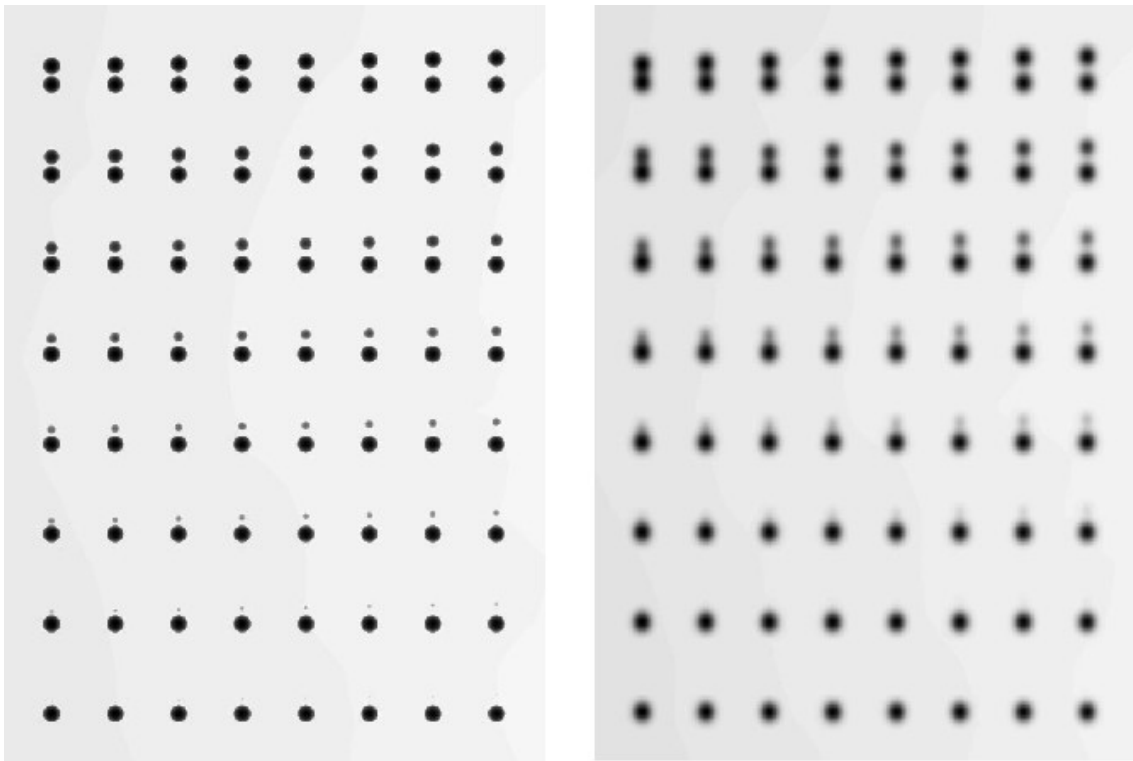


Figure II.7 Images of a 6 cm breast produced using a 25  $\mu\text{m}$  pixel detector.

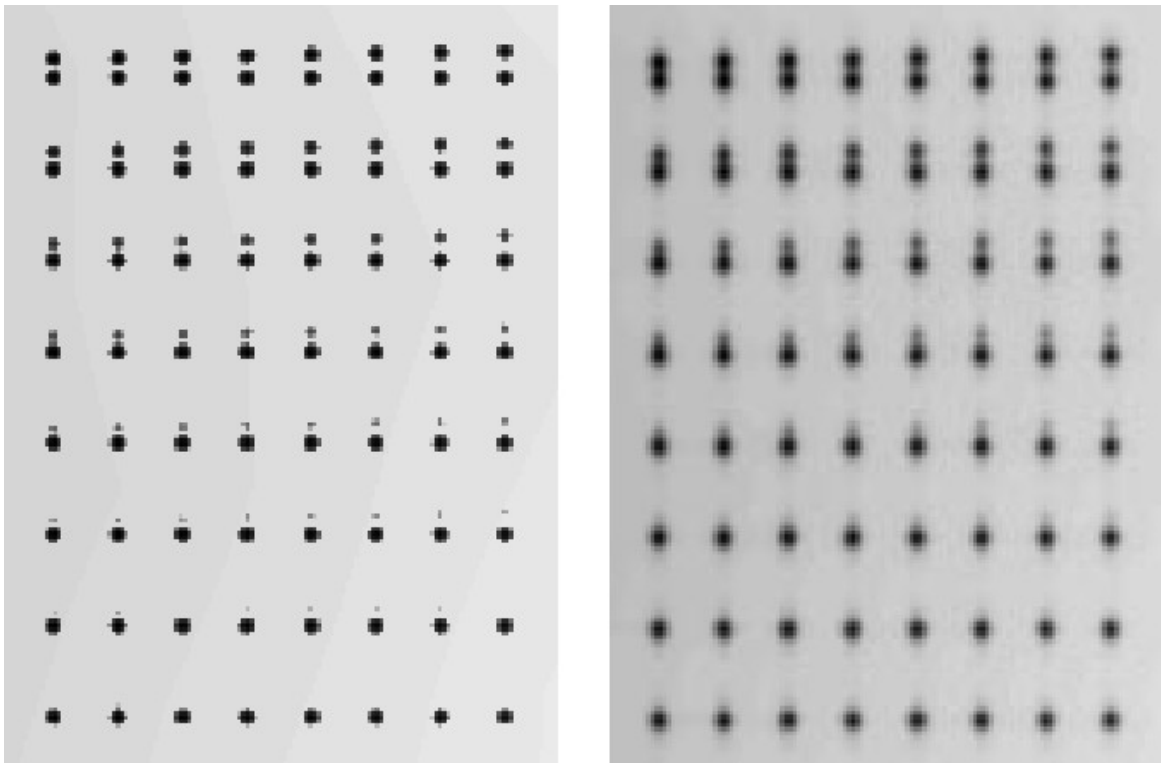


Figure II.8 Images of a 7 cm breast produced using a 100  $\mu\text{m}$  pixel detector.

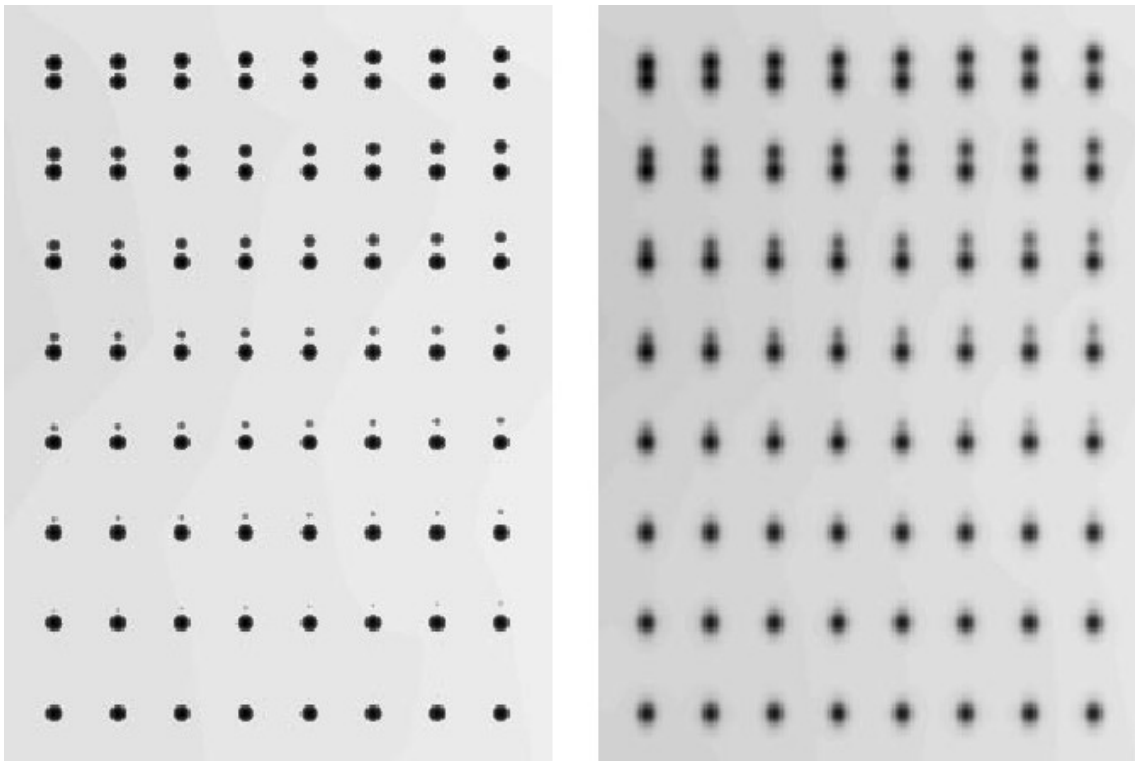


Figure II.9 Images of a 7 cm breast produced using a 50  $\mu\text{m}$  pixel detector.

## II.3 Image Analysis Codes

This section contains the two Matlab™ codes developed for image analysis. These codes incorporate the methods of analysis as described in Chapter 3. Sections II.3.1 and II.3.2 are the algorithm and Matlab™ script, respectively, for calculating image resolution. Sections II.3.3 and II.3.4 are the algorithm and Matlab™ script used for calculating the total image contrast.

### II.3.1 Algorithm for Calculating Resolution

1. Read in data from MCMIS output files
2. Set the center row of the top line of microcalcifications. All other centers for a row of microcalcifications will be determined according to this value.
3. Set 8 Regions of Interest (ROIs) around each row of microcalcifications based on the center for each row.
4. Loop through each of the 8 ROIs and determine how many microcalcifications are visible.
  - A. Calculate average pixel value for current ROI and minimum possible pixel value (mppv) that results in being outside a microcalcification.
  - B. Determine the minimum pixel value in each column of the current ROI.
  - C. Compare minimum for each column to the mppv for the ROI.
    - i. 0 for columns that have no pixels below mppv
    - ii. 1 for columns that have at least one pixel below mppv
  - D. Determine if the gradient between each column in the current ROI is positive, negative, or 0.
    - i. Add 1 to positive tally if gradient is positive.
    - ii. Add 1 to negative tally if gradient is negative.
  - E. Compare positive tally to negative tally.
    - i. If positive tally = negative tally, positive tally = number of visible microcalcifications
    - ii. If positive tally  $\neq$  negative tally, an error has occurred, choose new value of threshold for this ROI
  - F. Display either the number of visible calcifications, or an error message.

## II.3.2 Code for Calculating Resolution

```
function[con]=resolution(m,n,p,thresh)

%-----
% The purpose of this function is to calculate the resolution for a given MCMIS
% image, where resolution is defined as the total number of microcalcifications
% that can be detected within the image.
% inputs from the user: m    - number of pixels in y direction
%                       n    - number of pixels in x direction
%                       p    - pixel size (25, 50, or 100)
% output: The number of microcalcifications detected in each row, or if an
%         error has occurred for a row.
%-----

path(path,'/afs/eos/service/ne/project/ne_med/MCMIS/Matlab');

%-----
% read in necessary data from monte carlo output files.
%-----

if p==100
    un=binread('INPUT_FILE_1',m,n);
    xd=22; yd=15;
    xn=11; yn=8;
elseif p==50
    un=binread('INPUT_FILE_2',m,n);
    xd=44; yd=30;
    xn=22; yn=16;
else
    un=binread('INPUT_FILE_3',m,n);
    xd=88; yd=60;
    xn=44; yn=32;
end;

%-----

%-----
% set up center of first microcalcification row. this is the top row of the
% microcalcification image.
%-----
```

```

if p==100
    cj(1)=745;
elseif p==50
    cj(1)=388;
else
    cj(1)=474;
end;

%-----

%-----
% using center for location of microcalc row 1, set centers of remaining
% cluster rows.
%-----

for lcv1=2:8
    cj(lcv1)=cj(lcv1-1)+yd;
end;

%-----

% set boundaries for the width of the ROI
xmin = floor(0.10*n);
xmax = ceil(0.90*n);
xdim = xmax-xmin;

% loop through each row's ROI and determine the number of visible microcales
for lcv4=1:8

    % assign ROI pixel values to a matrix
    amat = un(cj(lcv4)-yn:cj(lcv4)+yn,xmin:xmax);

    % calculate average pixel value for the row ROI
    ap = mean(mean(amat));

    % calculate minimum possible pixel value to be considered "outside" a
    % microcalcification
    mppv = ap*thresh;

    % create a row vector of the minimum value for each column of pixels
    % in the current row ROI
    minval = min(amat);

    % create a row vector of "flags" for each column in the row, with each flag

```

```

% initialized to a value of 0. if any of the minimum values in the column
% fall below the mppv, assign the flag for that column a value of 1.
cf = zeros(1,xdim+1);
for lcv2=1:xdim+1
    if (minval(lcv2) < mppv)
        cf(lcv2) = 1;
    end;
end;

% create a positive gradient flag tally, a negative gradient flag tally, and
% another row vector of "flags" for the difference of each adjacent pair of
% pixels. subtract flags for adjacent columns. if the result is positive,
% add 1 to positive gradient tally. if the result is negative, add 1 to the
% negative gradient tally. after all gradients are determined for the row,
% compare the number of pgfs to ngfs. If they are equal, the number of either
% flag value is the number of microcalcification detected. If they are not
% equal, an error has occurred, and a new threshold must be chosen.
pgfs = 0.;
ngfs = 0.;
gf = zeros(1,xdim);
for lcv3=1:xdim
    gf(lcv3)=cf(lcv3)-cf(lcv3+1);
    if (gf(lcv3)>0)
        pgfs = pgfs+1;
    elseif (gf(lcv3)<0)
        ngfs = ngfs+1;
    end;
end;
if (pgfs==ngfs)
    display(['Row ' num2str(lcv4) ' has ' num2str(pgfs) ' visible calcifications.']);
else
    display(['Row ' num2str(lcv4) ' has an error.']);
end;
end;

```

### II.3.3 Algorithm for Calculating Contrast

1. Read in data from appropriate MCMIS output files and set any necessary dimensions not set by user.
2. Set ROI around entire microcalcification phantom.
3. Calculate average pixel value for current ROI and minimum possible pixel value (mppv) that results in being outside a microcalcification.

4. Compare each pixel in ROI to mppv.
  - i. If pixel value  $\geq$  mppv, add pixel value to outside tally.
  - ii. If pixel value  $<$  mppv, add pixel value to inside tally.
5. Calculate average outside value and average inside value.
6. Calculate contrast for entire image.

### II.3.4 Code for Calculating Contrast

```
function[con]=contrast(m,n,p,thresh,type)

%%%%%%%%%%%%%%%%%%%%%%%%%%%%%%%%%%%%%%%%%%%%%%%%%%%%%%%%%%%%%%%%%%%%%%%%
%
% The purpose of this function is to calculate the contrast for a given MCMIS image.
% Only images created using the Senoscan system phantom developed for the Zeigler
% thesis should be used with this function.
%
%%%%%%%%%%%%%%%%%%%%%%%%%%%%%%%%%%%%%%%%%%%%%%%%%%%%%%%%%%%%%%%%%%%%%%%%

path(path,'/afs/eos/service/ne/project/ne_med/MCMIS/Matlab');

%%%%%%%%%%%%%%%%%%%%%%%%%%%%%%%%%%%%%%%%%%%%%%%%%%%%%%%%%%%%%%%%%%%%%%%%
%
% Read in correct image file according to information given by user. Information given
% by user should include dimensions of image, pixel size, contrast threshold, and type of
% image, i.e. smeared or unsmeared images. Also set dimensions for ROI according to
% image type set by user.
%
%%%%%%%%%%%%%%%%%%%%%%%%%%%%%%%%%%%%%%%%%%%%%%%%%%%%%%%%%%%%%%%%%%%%%%%%

if type==0
  if p==100
    un=binread('INPUT_FILE_1',m,n);
    xd=22; yd=15; % fine mesh ROI x- and y-dimensions
    xn=11; yn=8; % coarse mesh ROI x- and y-dimensions
    xmin = 90;
    xmax = 273;
    xdim = xmax-xmin;
    ymin = 657;
    ymax = 789;
```

```

    ydim = ymax-ymin;
elseif p==50
    un=binread('INPUT_FILE_2',m,n);
    xd=44; yd=30;
    xn=22; yn=16;
    xmin = 179;
    xmax = 545;
    xdim = xmax-xmin;
    ymin = 323;
    ymax = 587;
    ydim = ymax-ymin;
else
    un=binread('INPUT_FILE_3',m,n);
    xd=88; yd=60;
    xn=44; yn=32;
    xmin = 85;
    xmax = 820;
    xdim = xmax-xmin;
    ymin = 376;
    ymax = 901;
    ydim = ymax-ymin;
end;
else
    if p==100
        mo=binread('INPUT_FILE_4',m,n);
        xd=22; yd=15;
        xn=11; yn=8;
        xmin = 90;
        xmax = 273;
        xdim = xmax-xmin;
        ymin = 657;
        ymax = 789;
        ydim = ymax-ymin;
    elseif p==50
        mo=binread('INPUT_FILE_5',m,n);
        xd=44; yd=30;
        xn=22; yn=16;
        xmin = 179;
        xmax = 545;
        xdim = xmax-xmin;
        ymin = 323;
        ymax = 587;
        ydim = ymax-ymin;
    else
        mo=binread('INPUT_FILE_6',m,n);

```

```

    xd=88; yd=60;
    xn=44; yn=32;
    xmin = 85;
    xmax = 820;
    xdim = xmax-xmin;
    ymin = 376;
    ymax = 901;
    ydim = ymax-ymin;
end;
end;

%%%%%%%%%%%%%%%%%%%%%%%%%%%%%%%%%%%%%%%%%%%%%%%%%%%%%%%%%%%%%%%%%%%%%%%%
%
% Read in image data to a matrix
%
%%%%%%%%%%%%%%%%%%%%%%%%%%%%%%%%%%%%%%%%%%%%%%%%%%%%%%%%%%%%%%%%%%%%%%%%

if type==0
    amat = un(ymin:ymax,xmin:xmax);
else
    amat = mo(ymin:ymax,xmin:xmax);
end;

%%%%%%%%%%%%%%%%%%%%%%%%%%%%%%%%%%%%%%%%%%%%%%%%%%%%%%%%%%%%%%%%%%%%%%%%
%
% (1) Determine average pixel value for entire ROI
% (2) Determine the minimum possible pixel value (mppv) for a pixel to be considered
%     outside of a microcalcification.
% (3) Compare every element in the image matrix to the mppv. If it falls below the
%     mppv, add it to the "inside" tally. If it is equal to or greater than the mppv, add it to
%     the "outside" tally.
% (4) Calculate the average value of pixels for both inside and outside tallies.
% (5) Calculate contrast for entire image.
%
%%%%%%%%%%%%%%%%%%%%%%%%%%%%%%%%%%%%%%%%%%%%%%%%%%%%%%%%%%%%%%%%%%%%%%%%

% (1) %
ap = mean(mean(amat));

% (2) %
mppv = ap*thresh;

% (3) %
inner_contrib = 0.;
inner_count = 0.;

```

```

outer_contrib = 0.;
outer_count = 0.;
for lcv2=1:xdim+1
    for lcv3=1:ydim+1
        if (amat(lcv3,lcv2) < mppv)
            inner_contrib = inner_contrib+amat(lcv3,lcv2);
            inner_count = inner_count+1;
        else
            outer_contrib = outer_contrib+amat(lcv3,lcv2);
            outer_count = outer_count+1;
        end;
    end;
end;

% (4) %
if (inner_count>0)
    inner_avg = inner_contrib/inner_count;
else
    inner_avg = 0;
end;
if (outer_count>0)
    outer_avg = outer_contrib/outer_count;
else
    outer_avg = 0;
end;

% (5) %
if (outer_avg == 0)
    image_contrast = 0.
elseif (inner_avg == 0)
    image_contrast = 0.
else
    image_contrast = abs(outer_avg - inner_avg)/(outer_avg + inner_avg)*2
end;

```